J. Fluid Mech. (1992), *vol.* 236, *pp.* 217–257
Printed in Great Britain

Structure of a particle-laden round jet

By ELLEN K. LONGMIRE[1] AND JOHN K. EATON[2]

[1] Department of Aerospace Engineering and Mechanics, University of Minnesota, Minneapolis, MN 55455, USA

[2] Department of Mechanical Engineering, Stanford University, Stanford, CA 94305, USA

(Received 7 February 1991 and in revised form 19 July 1991)

The interaction of solid particles with the temporal features of a turbulent flow has direct relevance to problems in particle and spray combustion and the processing of particulate solids. The object of the present study was to examine the behaviour of particles in a jet dominated by vortex ring structures. An axisymmetric air jet laden with 55 μm glass particles was forced axially with an acoustic speaker to organize the vortex ring structures rolling up in the free shear layer downstream of the nozzle exit. Visualization studies of forced and unforced flow with Reynolds number of the order of 20000 were completed using a pulsed copper vapour laser. Instantaneous photographs and videotapes of strobed forced flow show that particles become clustered in the saddle regions downstream of the vortex rings and are propelled away from the jet axis by the outwardly moving flow in these regions. Phase-averaged spatial distribution of particle number density computed from digitized photographs and phase-averaged particle velocity measurements yield further evidence that local particle dispersion and concentration are governed by convection due to large-scale turbulence structures. The large-scale structures and convection mechanisms were shown to persist for particle-to-air mass loading ratios up to 0.65.

1. Introduction

Many experiments have been performed on particle-laden jet flows including the recent work of Mostafa *et al.* (1989), Hardalupas, Taylor & Whitelaw (1989), and Fleckhaus, Hishida & Maeda (1987). These experiments have focused on providing time-averaged measurements in support of modelling efforts. Such quantities as the mean particle and fluid velocity profiles, mean particle concentration profiles, and turbulent Reynolds stresses have been measured. The results of these studies are useful for the development of models to predict the time-averaged behaviour of the jet but provide no information about the temporal features of the flow. For example, the time-averaged statistics yield little insight into the instantaneous interaction of particles and structures in turbulence.

In practical applications where solid or liquid particles must be injected into combustion chambers or process streams, the instantaneous rather than time-averaged distribution of the particles is often important. In a combusting or reacting flow, instantaneous particle concentration fields strongly influence local temperature and gas concentration levels. A particle in the middle of a dense cluster can experience a reaction environment which is radically different from that for a particle located far from any others. Since the dependence of reaction rates on temperature and concentration is often highly nonlinear, non-uniform particle concentrations could have substantial effects on both reaction rates and yields. Also, clusters of particles may damp or distort turbulent eddies in ways that evenly distributed

particles could not. Thus mixing characteristics in the carrier phase could be modified significantly. Models based on time-averaged behaviour cannot account for these effects.

The work in particle-laden jets contrasts sharply with recent work in single-phase jets which has focused on temporal structure. It has been well documented, beginning with Crow & Champagne (1971), that large-scale vortex rings, which roll up quasi-periodically downstream of the jet nozzle exit as a result of the Kelvin–Helmholtz instability, dominate the structure of single-phase jets up to x/D of about 4. Beyond this axial location, organized helical structures also become important (see Petersen & Samet 1988). Even in the far field of turbulent jets, large-scale structures have been shown to have a strong influence on mixing and entrainment (see Dahm & Dimotakis 1987). The present study attempts to extend the understanding of single-phase jets to gas jets laden with solid particles. In particular, we wish to determine the effects of the vortex ring structures on the instantaneous particle concentration and velocity fields.

The inertia of a particle can be assessed quantitatively by calculating a particle time constant. Assuming Stokes flow and particle number density much greater than the fluid density, the particle time constant is

$$\tau_p = \frac{\rho_p d_p^2}{18\mu},$$

where d_p is the particle diameter, ρ_p is the particle density and μ is the fluid viscosity. For larger particles, empirical drag laws must be used to calculate a time constant. The particle response to turbulent velocity fluctuations is governed by the Stokes number γ, i.e. the ratio of the particle time constant to an appropriate fluid timescale. A fluid timescale τ_f based on a given eddy can be determined such that

$$\tau_f = \frac{L_v}{U_v},$$

where L_v is an eddy lengthscale and U_v is an eddy velocity scale. If we relate the time scales of the fluid and particles, we can divide the possibilities of particle response to turbulent flow into three regimes. First, if $\tau_p \gg \tau_f$, a particle will not respond to fluctuations in the flow. On the other hand, if $\tau_p \ll \tau_f$, a particle would respond completely to the flow, following any fluctuations. In laser-Doppler anemometry experiments, seed particles are assumed to behave in this manner.

The third possible regime occurs when τ_p and τ_f are of the same order of magnitude. In this case, particles respond partially to fluctuations in the flow. The particles cannot follow fluid elements exactly, but their paths are altered by fluid fluctuations. Flow in this regime is the most poorly understood and therefore the most difficult to model. Also, many of the practical applications of particle-laden flow fall within this category. Thus, the present experiment attempts to investigate flow in this regime.

Experimental results in two-dimensional mixing layers (Kobayashi *et al.* 1987; Kamalu *et al.* 1988; Lazaro & Lasheras 1989) suggest that for particles of appropriate timescale, large-scale vortical structures do affect particle dispersion. In all three sets of experiments, the Stokes number varied approximately between 10 and 1 over the regions studied with τ_f based on the characteristic eddy turnover scale of the mixing layer $\delta/\Delta U$. A common conclusion was that particle concentrations were much higher in the vortex braid regions than in the vortex core regions. Also, time-averaged LDA

measurements of transverse velocities showed that glass particles tended to move away from the centre of the mixing layer as opposed to fluid elements which moved toward it. These results confirmed the idea of Crowe, Gore & Troutt (1985) that particles of intermediate time constant could be caught up in the outer regions of the dominant vortex structures and flung into the free stream. Owing to the interaction of the particles with these structures, it would then be possible for particles to disperse faster than fluid elements.

Models that have examined the interaction of particles and flow structure can be divided into two categories: models of homogeneous or isotropic turbulence, and models of free shear flows. Maxey (1987) studied particle settling under the influence of gravity in homogeneous turbulence. Numerical simulations of two-dimensional, incompressible, periodic flow containing small particles showed that particle settling velocities were greater than those in still fluid. Asymptotic analyses revealed the most important mechanism for this behaviour : the particle flow field is compressible, where $\nabla \cdot \boldsymbol{v} > 0$ in regions of high vorticity or low strain rate, and $\nabla \cdot \boldsymbol{v} < 0$ in regions of high strain rate ($\boldsymbol{v}$ is the particle velocity vector). Thus the particles tend to accumulate in the regions of high strain rate. In Maxey's flow field, the effect of this bias was to cause particles to settle more rapidly than would particles in still fluid.

Squires & Eaton (1991) performed direct numerical simulations on isotropic turbulence containing small dense particles. Over the range of cases studied, particle dispersion was maximized for $\gamma = \tau_p/\tau_f$ of 0.28. Particle eddy diffusivity was greater than fluid element diffusivity for all of the cases studied. Squires & Eaton (1991) found results similar to Maxey (1987) in that intermediate-sized particles tended to collect in regions of low vorticity and high strain rate. In one simulation the maximum particle number density measured was 30 times the mean. In general, particle number density was smaller than the mean in regions of high vorticity.

Chein & Chung (1987) and Chung & Troutt (1988) looked at particles in two-dimensional mixing layers and axisymmetric jets respectively using inviscid vortex methods. In both cases, the flow was modelled by small discrete vortices which precess in space according to induced velocities. Large-scale structures similar to those seen in experiments developed in the flow. In the two-dimensional model, particles were injected into a flow with pairing vortices. Particles associated with Stokes numbers from 0.5–5 were found to be capable of greater lateral dispersion than fluid elements. For $\gamma = 0.5$, particles interacting with the pairing vortices were more likely to be flung outward than particles interacting with an already paired vortex of the same strength. Finally, distributions of particles were computed across the mixing layer. The distributions were bimodal rather than Gaussian for all but the heaviest particles tested.

The jet simulation was run for Stokes numbers (γ_τ) of 0.05, 1, 10 and 100 where τ_f was assumed to be constant at D/U_0 and D and U_0 are jet exit diameter and initial velocity respectively. Lateral dispersion was quantified according to the square of the difference between a particle's radial position at a given time and its initial radial position. This criterion was applied at a fixed time for particles initiating near $r/D = 0.45$. According to this criterion, which did not differentiate between particles which had moved inward and particles which had moved outward, particles with time constants yielding $\gamma = 1$ exhibited the greatest dispersion. As in the experimental studies, these particles tended to wrap around the outer edges of the cores of the large vortices. For the same initial flow conditions, the $\gamma = 10$ case appears to show the largest percentage of particles which have moved toward the jet axis. When the simulation was cut off, some of these particles were distributed in the

vortex braid regions and appeared as if they would continue moving away from the jet axis if the simulation were continued. Unfortunately, no particle velocities were reported. Similar particles starting closer to the jet axis were less likely to move outward than particles starting near the nozzle edge.

The experiments and models described above have provided useful information about how particle motion is related to flow structures, but more quantitative data especially on jet flows is needed. The objective of this work was thus to examine the instantaneous structure of the near field of a particle-laden jet. Are the flow structures in particle-laden jets the same as those in single-phase jets? How are the particles dispersed or concentrated within the jet, and how do particle velocities vary in the vicinity of vortex ring structures? Finally, how does variation of particle loading affect the flow structure?

For the current experiments, a round low-speed air jet was chosen because of its simplicity and similarity to previously studied single-phase jets. The jet was loaded with glass particles sized between 50 and 60 μm yielding a particle timescale of about 21 ms. The jet was forced at specific frequencies in order to generate vortex rings of different scales. In this manner, the ratio of particle to fluid timescales could be varied systematically. In one set of experiments the flow was forced with two frequencies simultaneously to cause a pairing of vortex rings in order to examine the effect of the pairing on particle dispersion. To isolate the effects of flow structures on the particles, most experiments were performed at fairly low particle mass loadings (5–12% mass of particles to mass of air). The mass loading was increased substantially, however, in one series of tests to examine the reverse effect: that of the particle loading on flow structure.

2. Experimental facility

The primary objective in the design of the flow apparatus was to obtain a steady flow of particles and air at the jet exit with a nearly top-hat-shaped air velocity profile and as near as possible to a uniform particle distribution. The apparatus was modified several times as the experiments became more quantitative and the requirements for steady flow over longer periods of time became more stringent.

The basic air flow supply system as sketched in figure 1 was the same for all versions of the apparatus. Pressurized air was supplied by a compressor. A pressure regulator was used to set the total air flow rate which was measured with a rotameter calibrated according to the rotameter inlet temperature and pressure. Uncertainty in the mean total air mass flow rate was $\pm 1\%$ owing to unsteadiness over longer timescales (~ 2 min). After the flow meter, the air line split allowing three parallel paths for the air flow. Air could pass through a particle-laden fluidized bed, a primary bypass line, or a secondary bypass line containing a smoke generation system. The three lines reconnected downstream of the fluidized bed and smoke generator. The flow continued downstream toward the jet plenum. A tee split the flow symmetrically, and air and particles entered the plenum through two diametrically opposed, horizontally oriented $\frac{3}{4}$ in. diameter PVC pipes.

The original jet apparatus (Jet 1) is sketched in figure 2. The plenum was constructed in two sections from PVC pipe with 4 in. nominal inner diameter. A perforated plate, inserted to help make the flow more uniform, was located between the plenum sections. Two aluminium rings were placed between the downstream PVC section and the jet nozzle. Originally two fine-mesh screens were stretched across these rings, but they were removed since they tended to become clogged with

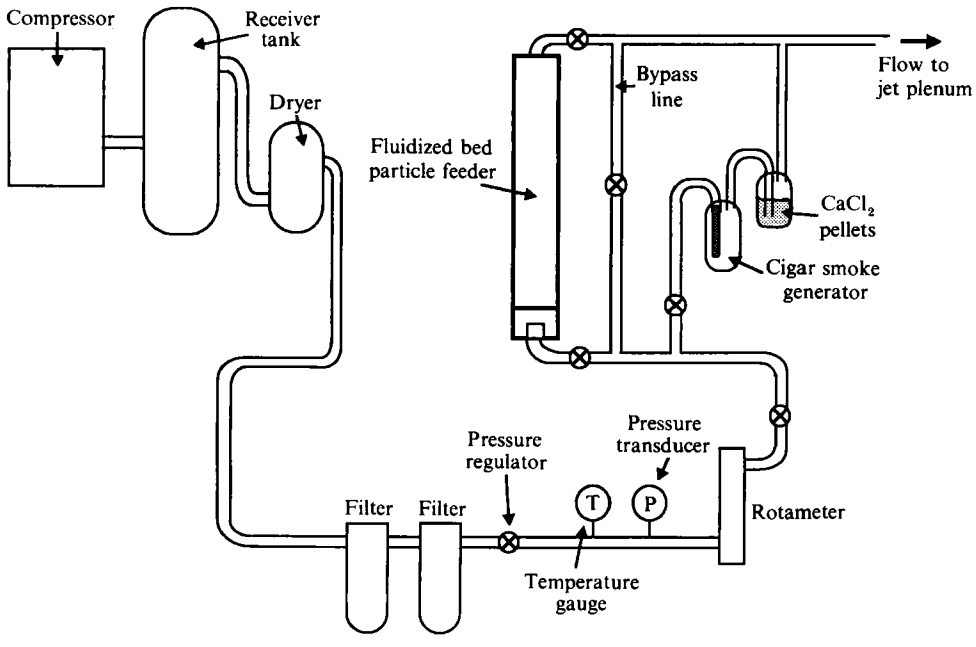

FIGURE 1. Schematic of air and particle feed system.

particles. Measurements of velocity profiles and spectra with a hot wire indicated no significant differences in turbulence level or spectral content whether or not the screens were present. Also, measurements of azimuthal velocity taken with a single-component LDA system revealed no significant swirl in the jet. An audio speaker attached to a Plexiglas flange formed the upstream end of the plenum.

The flow was accelerated through a transparent Plexiglas nozzle with a 25.8 : 1 area ratio contraction and an exit diameter of 2 cm. The contraction length was 4.5 in. The contraction profile was generated from a fifth-order polynomial with zero slope and curvature at inlet and outlet. For the studies involving unforced flow and strobed visualization (§§4.1 and 4.2.1), the flow was directed vertically upward. Later the jet orientation was inverted and the flow directed vertically downward to eliminate particle accumulation within the plenum. The change in orientation had no noticeable effect on the flow structure. The experiments involving variation of particle loading were performed with this configuration.

To alleviate problems of particles flying toward the jet axis downstream of the nozzle exit and particles accumulating on the nozzle inner surface, a second plenum–nozzle combination (Jet 2 in figure 2) was constructed and used for the studies on particle velocity and number density. This new plenum had a nominal inner diameter of 2 in. The set-up of Jet 2 was similar to the original one. A contraction connected the 4.5 in. diameter speaker to the smaller plenum. A piece of cloth was stretched across the plenum at the downstream end of this contraction to prevent particle build-up. Again, the plenum was constructed from two sections of 2 in. PVC pipe. The perforated plate inserted between the two plenum sections was removed for the LDA measurements because particles tended to pile up on the plate over longer periods of time. Also, a splitter plate of 0.065 in. thickness was inserted between the two flow inlets for the LDA measurements. The splitter plate, which measured 2.375 in. in length and 2 in. in width, extended from the speaker contraction exit to 0.875 in. downstream of the flow inlets. This also improved flow

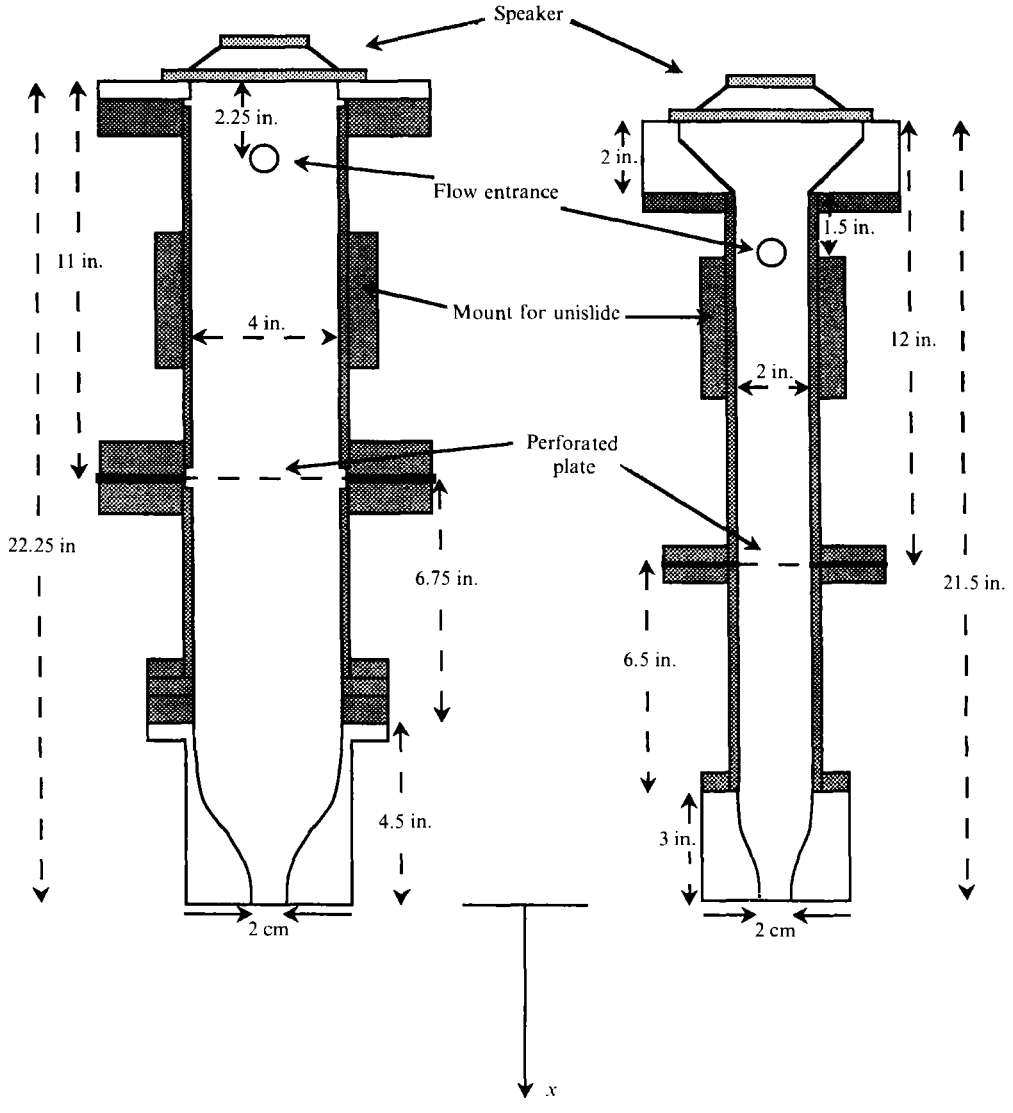

FIGURE 2. Schematics of Jet 1 and Jet 2.

steadiness over long periods of time by preventing unstable interaction of the flow from the opposing jets entering the plenum.

The Plexiglas nozzle had a 6.45 : 1 area ratio contraction between the plenum and the 2 cm diameter exit. The length of this nozzle was 3 in., and again the profile was generated from a fifth-order polynomial with zero slope and curvature at inlet and outlet. The flow from this apparatus was always directed vertically downward. Typical nozzle exit velocities for both Jet 1 and 2 were 14.4 m/s and 17.0 m/s yielding jet Reynolds numbers (Re_D) of 19000 and 23000. Qualification studies on the single-phase unforced jets with a hot wire showed top-hat shaped profiles at each nozzle exit with turbulence levels in the core region of about 1%.

It is worth mentioning that neither nozzle precisely represented a 'standard' jet geometry where the two standard geometries are a jet emerging from an infinite plane and a jet emerging from a thin, sharp-edged nozzle. The latter allows

entrainment from upstream of the nozzle exit while the former does not. Using Jet 1, the effect of this initial condition was tested against one where the solid exit plane extended beyond $15D$ in all directions. Visualization of smoke-marked and particle-laden flow showed that the two different initial conditions did not yield significantly different flow patterns close to the jet.

For both jets, a standard 4.5 in. diameter 4 Ω audio speaker (Yamaha YCS 500) was attached to the upstream end of the plenum in order to introduce velocity perturbations at the jet exit. In Jet 1, the speaker mouth was covered with tightly-stretched cloth to protect it from particles. The amplitude and frequency of the speaker motion could be controlled to produce any desired waveform or perturbation at the jet exit. An IBM XT personal computer containing a Data Translation 2801 data acquisition and control card generated the forcing waveforms. The analog signals were sent through a low-pass filter and a standard audio amplifier before reaching the speaker. The forcing was generally high amplitude to organize the vorticity flux and the resulting vortex ring structure.

Since the overall response of the amplifier/speaker/plenum system could not be predicted *a priori*, the waveform of the axial jet exit velocity was measured for each case studied. Mean and fluctuating velocities were measured and power spectral density functions computed. In general, the flow was forced at large amplitudes to impose a strong oscillating component on the mean velocity. In the forced cases, the spectra were completely dominated by sharp peaks at the forcing frequency. Forcing amplitudes and resulting r.m.s. velocity fluctuations for the various forcing cases are listed in §4. When the jet was not forced, the velocity fluctuation levels in the core region were less than 1%.

The particles used in the current experiments were glass beads nominally sized between 50 and 60 μm using an air classifier. Nearly all of the particles were spherical although a few irregularly shaped shards were present. A Coulter counter and a sonic sifter were employed to determine the actual distribution of particle sizes. About 83% of the particle mass fell between 50 and 60 μm, and 95% of the mass fell between 45 and 65 μm. Average particle density was measured as 2.4 g/cm^3. The particle density above yields timescales τ_p of 18–26 ms for particles with diameters between 50 and 60 μm.

The particles were loaded into a fluidized bed with 6 in. × 6 in. cross-section and 34 in. total bed and freeboard height. Air was injected into the bed through a porous, sintered bronze plate dividing the freeboard and windbox. Particles which elutriated out of the top of the bed were fed to the jet plemun. The mass loading ratio (M) of particles to air in the flow could be varied from zero to 1.0 by varying the total volume of particles in the bed and the relative amount of air flowing through the bed and the bypass line. Runs were limited to short times (15–20 min) under these conditions, because the mass loading would slowly decrease as the bed height dropped.

Data were acquired using a Data Translation 2801 board contained in an IBM XT personal computer. When simultaneous data acquisition and instrument control were required, two IBM XT computers, each containing a DT 2801 board, were used. One computer acquired data while the other delivered control signals. Speaker forcing and laser pulsing signals were sent out on 12-bit digital-to-analog output channels using the direct memory access (DMA) option.

3. Experimental techniques

3.1. *Flow visualization*

Two methods were employed to mark the jet air flow. To seed the air in unforced and in particle-laden flow, cigar smoke was fed through a secondary bypass line in parallel with the fluidized bed and primary air bypass. (See figure 1.) Air was forced directly through a burning cigar into a small mixing chamber and then bubbled through calcium chloride pellets in a second chamber before it merged with the primary air and particles. The smoke was well mixed with the air before it reached the jet nozzle. The smoke particles were assumed to have diameters of the order of 1 μm and appeared to follow all scales of the fluid flow. This method provided dense smoke for short periods of time, but did not work consistently. A Concept Comet 4 smoke generator provided more consistent glycerine smoke, but could be used only for single-phase flow owing to clogging problems. The glycerine smoke was fed into the air line through a Plexiglas venturi upstream of the jet plenum. The venturi was inserted for the smoke visualization studies only, and the volumetric flow rate of smoke-seeded air into the throat was accounted for in determining the total mass flow eventually exiting the jet. These smoke particles appeared to follow all scales of the fluid flow initially but, once in the centres of large vortex cores, the particles either broke up or migrated outward by a small distance. Hence the very centres of vortex cores in forced flow often appear devoid of smoke. Analysis of photographs and comparison with the numerical model of Chung & Troutt (1988) suggest that some of the smoke particles could have been as large as 5 μm yielding time constants too large to track all fluid elements faithfully. Since we were mostly concerned with marking large-scale structures in visualizing the air phase, however, these larger smoke particles were still appropriate for our experiments.

A Plasma Kinetics 151 copper vapour laser was used for illumination of both smoke and particles. The laser generated green light pulses of approximately 30 ns duration which individually could freeze all scales of the flow. The 1 in. diameter beam passed through a 400 mm focal length cylindrical lens and a 1 m focal length spherical lens to form a thin (1 mm) sheet of light perpendicular to the jet nozzle exit. The normal operating pulsing frequency of the laser of 5600 Hz could be reduced or altered as needed for several minutes at a time.

Instantaneous flow field images were photographed with a Nikon FE2 35 mm camera and a Nikkor 2.8, 55 mm micro lens attached to an MD-12 motor drive with an electronic trigger. The lens was found to produce no measurable distortion of the field of view in the focal plane.

For the strobed smoke and particle visualization studies, the laser pulsing and jet speaker forcing frequencies were coupled. Interlaced arrays containing the speaker waveform and laser triggering pulse were stored in the IBM XT. Values in the arrays were then sent out alternately to the speaker and laser through two D/A channels. The DT 2801 board clock controlled the output frequency of the waveform and the laser pulse. With this method, the laser could be pulsed continuously at the same phase of the forcing waveform to 'freeze' the flow. Also, the phase of the laser pulse could be changed gradually to cause the illuminated flow to precess forward slowly in time. Strobed flow was captured on videotape using a JVC Model GR-C1U video camera framing at a rate of 30 Hz. Therefore, each frame of videotape contained a superposition of a number of images depending on the laser pulsing frequency.

Single-pulse, phase-locked, laser-illuminated photographs were obtained using a specially constructed circuit to link the laser-pulse and speaker timing with that of

the 35 mm camera. This circuit was necessary because a significant delay (= 92 ms) occurred between the time the camera was electronically triggered and the time the shutter actually opened. The instrumentation set-up and electronic timing diagram are described in detail in Longmire & Eaton (1990).

3.2. *Particle number density measurements*

For the quantitative number density measurements, the jet was operated at a low mass loading (5–11%) providing a relatively low number density to facilitate the identification of individual particles. Single pulse photographs were obtained at known forcing phases. To provide reference points for data analysis, three illuminated pinholes were located the same optical distance from the camera as the laser sheet and imaged onto the focal plane with a mirror. Photographs were printed on 8 in. × 10 in. sheets of paper so that individual particles could be identified easily.

Each printed photograph was scanned to produce a binary image matrix using a DEST PC Scan 1000 scanner interfaced with a Macintosh II computer. Software first decoded the image matrix into the corresponding full bit map representation. A second routine searched the bit map file to identify all contiguous objects and computed each object's centroid, pixel area, and moment of inertia. These values were then used as criteria for identifying particles, fiducial marks, and stray objects. The area (number of pixels in an object) could vary for a single particle from 1 up to about 50 depending on the particle's position within the laser sheet, because scattering from particles in the centre of the sheet was much more intense than that from particles near the sheet's edges. The moment of inertia criterion was used to differentiate round objects from elongated ones. In combination, the area and moment of inertia were used to identify not only individual particles, but also overlapping ones. Hence number density in areas of high particle concentration would not be underestimated. Once the fiducial marks and particles were found, the entire system was translated into real-scale coordinates.

Files of particle positions were converted into two-dimensional maps of number density. A rectangular grid of points spaced at 2 mm intervals served as the basis for the map. The number density at each of the four grid points surrounding each particle was incremented according to the exact particle position. For example, if the particle was equidistant from the four nearest grid points, the number density associated with each point was incremented by 1/4. Each map was normalized by the total number of particles counted. Photographs covered the range of x/D between 0 and 8 and typically contained about 1700 particles. In order to produce smooth mappings, the results from 25 photographs were summed and normalized for each case and phase of flow studied.

3.3. *Laser-Doppler anemometry*

To measure particle velocities in the flow, a single-component laser-Doppler anemometry system was employed. The system, set up to operate in back scatter, is sketched in figure 3. The beam splitter could be rotated so that either axial (V_x) or radial (V_r) particle velocities could be determined. A beam expander was required in order to shorten the measuring volume to an acceptable value. The resulting measuring volume had length and diameter of 0.38 mm and 0.053 mm respectively. Bragg shifting of one beam was used for the radial velocity measurements only as no reversing flow of particles occurred in the axial direction. The focusing lens and final mirror in the beam path were mounted on a horizontal motor-driven traverse allowing movement of the measuring volume in the radial direction. The entire LDA

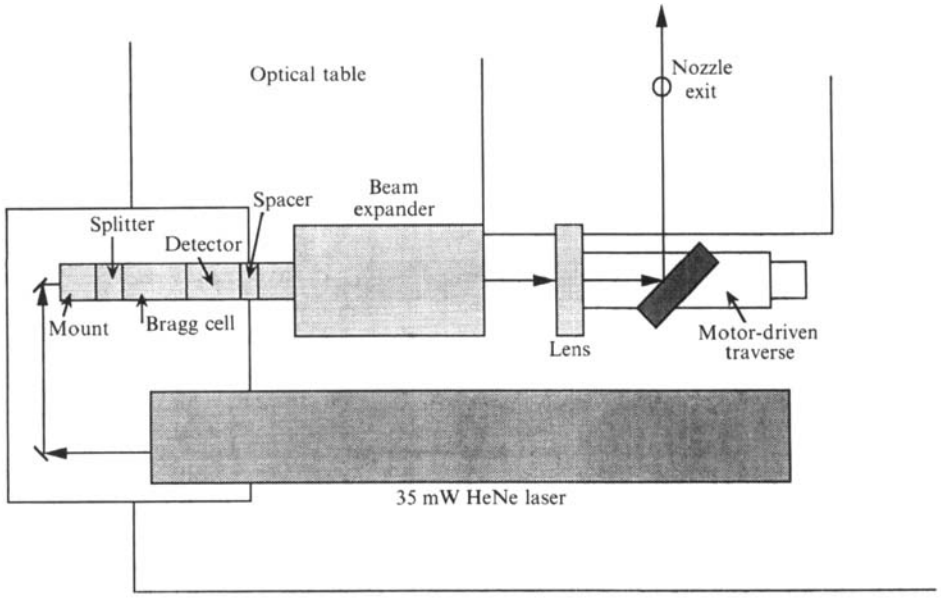

FIGURE 3. Overhead view of LDA set-up.

system was covered with a Plexiglas box to protect it from the particles. Uncertainty in single velocity measurements from all sources (chiefly flow unsteadiness) was estimated at 4%. This estimate was derived from repeated attempts to measure the same quantity on different occasions.

Time-averaged velocity measurements were computed by acquiring 2000 samples from the counter processor at a frequency of 20 Hz. Data rates near the jet centreline were in the range 400–1200 counts per second. Radial traverses moving away from the jet axis were cut off when the data rate dropped below 20 counts per second. Near the jet centreline, where the data rates were high, it is expected that velocities of particles were measured at random times compared with the passage of vortex ring structures. Near $r/D = 0.5$, however, where data rates were low, velocities of particles from areas of high concentration were measured preferentially. This occurred because the counter processor held the data from the last particle passing through the measuring volume until a new one arrived. Thus, if many more particles were present in vortex braid regions than in vortex cores, and the data rate was of the same order as the sampling rate, almost no particles present in the core regions would be sampled. Maximum values of statistical uncertainties in time-averaged mean velocity measurements were 0.6% for axial particle velocities and 0.05 m/s for radial particle velocities. The uncertainty in the variance was 6% for both axial and radial velocity measurements. The total uncertainty in mean time-averaged velocity measurements then, dominated by the uncertainty due to flow unsteadiness, was 4%

A timing box was constructed for taking phase-averaged velocity measurements. In this case, the phase-specific pulsing signal corresponding to the speaker forcing waveform was fed into the timing box. This signal was modified to yield an active phase bin of 15° (4.2%) of the forcing cycle. (For a forcing frequency of 360 Hz, the case studied, this bin size yields a sharper spatial resolution then the particle number density maps.) Variations in mean axial and radial velocity over this phase bin at a given point in space were estimated as 0.04 m/s or 0.4% and 0.017 m/s respectively (both considered negligible). The Data Ready line (DR), which outputs a short pulse

for each Doppler burst counted, was also connected to the timing box. Whenever the DR and Phase Bin signals were both high, the Data Translation board was triggered externally to read the digital input port. The counter processor was inhibited from updating while the digital input lines were read.

Phase-averaged velocity measurements contained either 1000 or 2000 samples per point. On radial traverses, measurements were cut off when fewer than 1000 counts were registered after 10 min of sampling. If the outermost point contained more than 800 samples, it was retained in the profile. For phase-averaged velocities measured on the jet centreline (2000 samples per point), maximum uncertainties due to statistical error were 0.5% for the mean and 6% for the variance. The maximum statistical uncertainty in determining mean phase-averaged velocity vectors (1000 samples per point) over a portion of the jet was 0.1 m/s (less than 1%). Thus, the statistical uncertainties in mean phase-averaged velocities were also negligible compared with the uncertainty due to flow unsteadiness, making the total uncertainty again 4%.

4. Results

A cylindrical coordinate system (x, r) with the origin on the jet centreline at the nozzle exit is used for all data presentation. In most of the plots in this section, these coordinates are normalized by the nozzle exit diameter D of 2 cm. The mean and r.m.s. fluid velocities are defined by U and u', and the mean and r.m.s. particle velocities are defined by V and v' respectively. Note that v' represents the standard deviation of the particle velocity and not a 'fluctuating' particle velocity.

The strobed smoke and particle visualizations described in §4.2.1 were performed at $Re_D = 23000$, and all other experiments were performed at $Re_D = 19000$. The mass loading ratio of particles to air ranged from 5 to 12%. Jet forcing frequencies ranged from $St_D = 0.3$ to 1.1, where $St_D = fD/U$ is the Strouhal number based on nozzle exit velocity and diameter.

4.1 *Structure of unforced yet flow*

A photograph of an instantaneous, two-dimensional slice of smoke-seeded, unforced single-phase flow is depicted in figure 4. Just downstream of the nozzle exit, the jet flow is divided from the surrounding air by a sharp interface. The inner jet fluid interacts with the surrounding outer fluid via the series of vortex rings which have rolled up beginning at $x/D \approx 0.8$. The spacing between rings is somewhat irregular, but the ring formation frequency is on the order of 1000 Hz. At $x/D = 2.7$, two vortices have paired into a larger ring. The jet core erodes gradually until it disappears suddenly at $x/D = 4.9$.

Figure 5 exhibits a photograph of unforced particle-laden flow. The glass beads appear as white dots against the grey background of the smoke-seeded flow. The fluid structure is very similar to that seen in the single-phase flow. Again, vortical structures roll up around the perimeter of the jet, and smaller vortices pair to form larger ones. The core breaks down at x/D of about 4.5. The glass particles in figure 5 are not evenly distributed as they exit the nozzle. Most of the particles are concentrated within the inner two thirds of the jet, and very few particles appear near the shear layer. The particle paths are mostly unaffected by the smaller vortices near the nozzle exit, but some particles are drawn away from the jet axis by the larger vortices downstream. These particles are present in the smoke-marked tongues of fluid on the downstream edges of the larger vortices. Near the end of the jet core, a large structure breaks up the stream of particles. Hence, coherent, large-scale flow

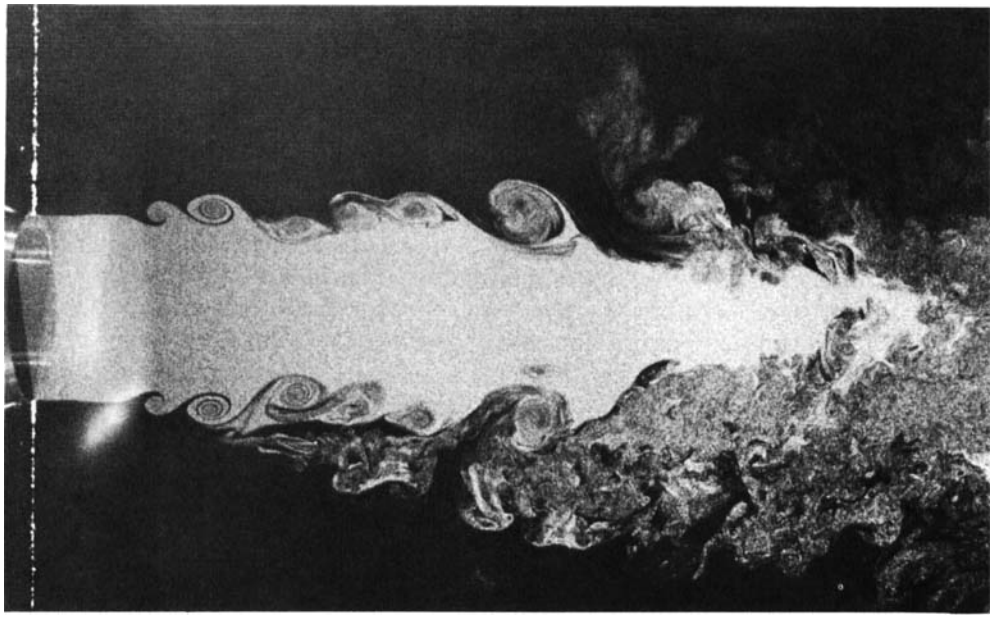

FIGURE 4. Unforced single-phase flow. $Re_D = 19000$.

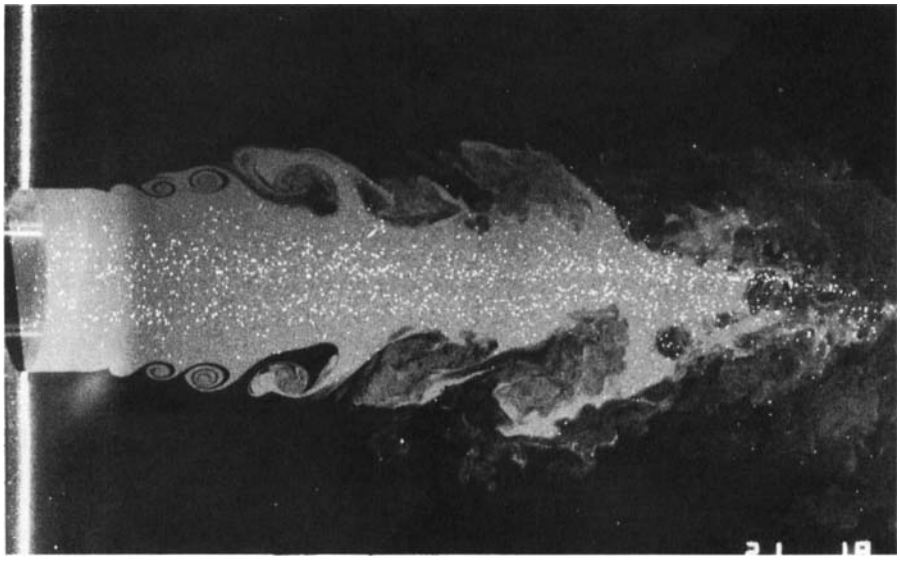

FIGURE 5. Unforced particle-laden flow. $Re_D = 19000$.

structures exist in particle-laden as well as single-phase jets, and the influence of the structures on altering or determining particle paths is evident.

4.2. *Structure of forced flow*

4.2.1. *Flow visualization studies*

Jet 1 was forced over a range of frequencies ($St_D = 0.26$–0.93) to produce different sizes of vortex rings in the axisymmetric shear layer. The forcing frequencies and core velocity fluctuations levels are listed in table 1. The flow was originally forced

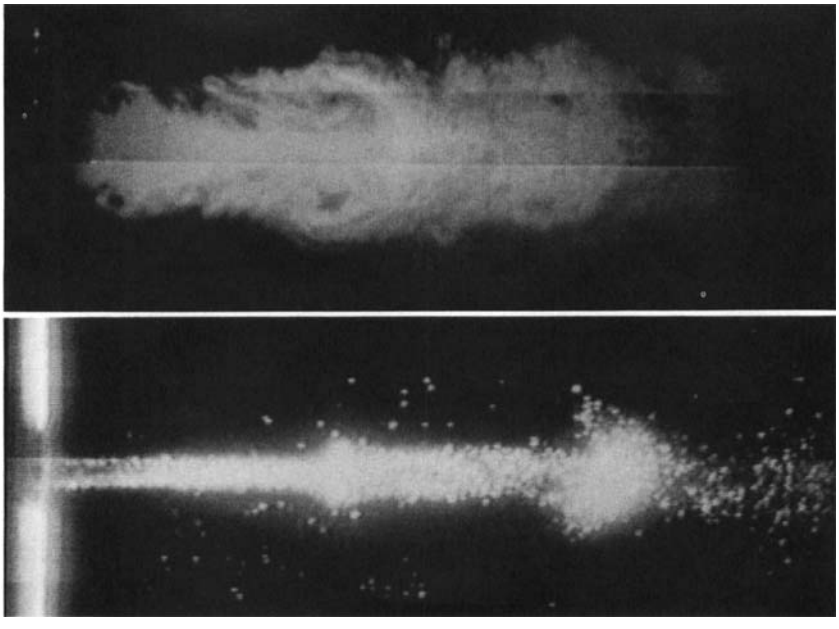

FIGURE 6. Single-phase and particle-laden flow, $St_D = 0.26$, $Re_D = 23000$.

Frequency (Hz)	St_D	u'/U
218	0.26	0.14
364	0.43	0.26
648	0.76	0.038
794	0.93	0.013
362+181(0)	0.43+0.21	0.21

TABLE 1. Forcing amplitudes for Jet 1, §4.2.1

at large amplitudes, but in subsequent studies the amplitudes were reduced to the minimum levels needed to induce the formation of vortices at the forcing frequency. Results from visualization studies of this flow are shown in figures 6–9. All of the photographs were taken from videotapes in which the laser was strobed at the jet forcing frequency. Therefore, they depict superpositions of a number of images. Each figure shows smoke-marked single-phase flow at $Re_D = 23000$ next to particle-laden flow with the same Reynolds and Strouhal numbers. The phases of the flow in each pair of photographs are not correlated as the strobing phase of the laser was precessed gradually through the forcing cycle for each section of videotape.

In figures 6 and 7, where the flow was forced at low frequencies ($St_D = 0.26$ and 0.43), the smoke-seeded images show large vortex rings forming at the forcing frequency. In the $St_D = 0.26$ case, the forcing frequency is so low that a very large forcing amplitude was required to generate repeatable structures with such a large axial spacing. In both figures, the spacing between the large structures remains constant as they move downstream. The corresponding images of particle-laden flow show that the presence of these structures strongly affects particle motion. In both figures, dense clusters of particles occur at the same frequency as the vortex formation frequency. These clusters are located in the regions of high strain

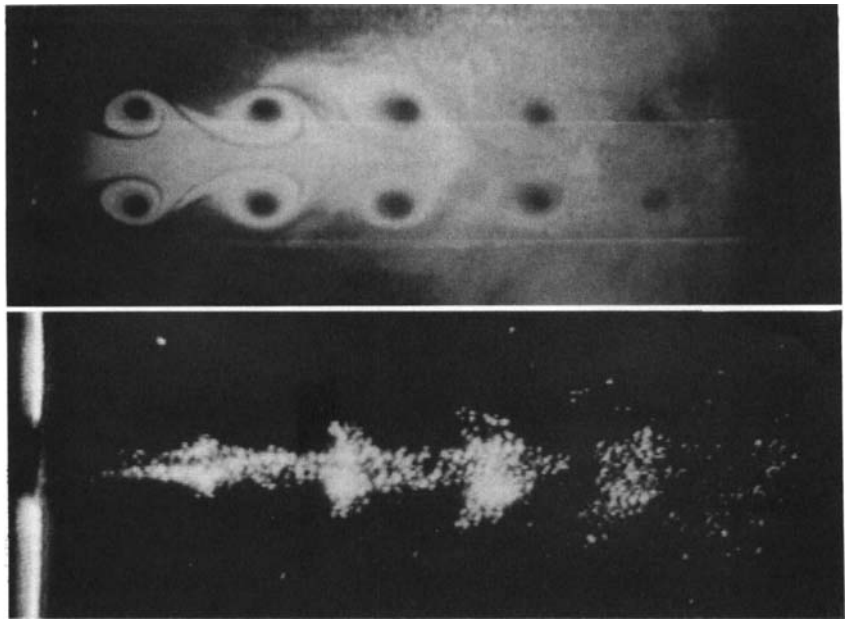

FIGURE 7. Single-phase and particle-laden flow, $St_D = 0.43$, $Re_D = 23000$.

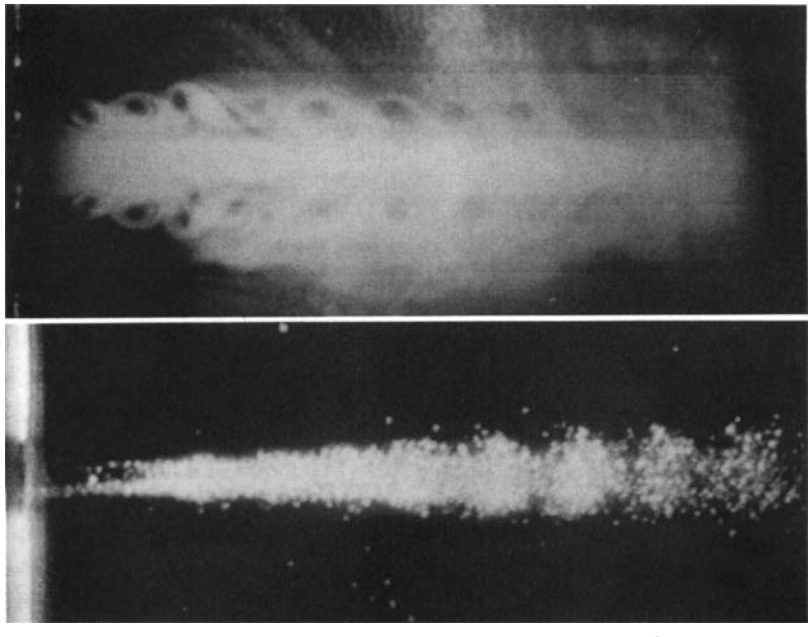

FIGURE 8. Single-phase and particle-laden flow, $St_D = 0.76$, $Re_D = 23000$.

immediately downstream of the vortex rings. (We know this from observing videotapes of flow seeded with both smoke and glass beads. Although the quality of the images was poor, the location of particle clusters relative to the vortex rings was clear.) The videotapes show consistently that particles are convected away from the jet axis by the outwardly moving fluid at these points. The particles gain radial momentum from the fluid and are propelled outward. Possessing too much inertia to

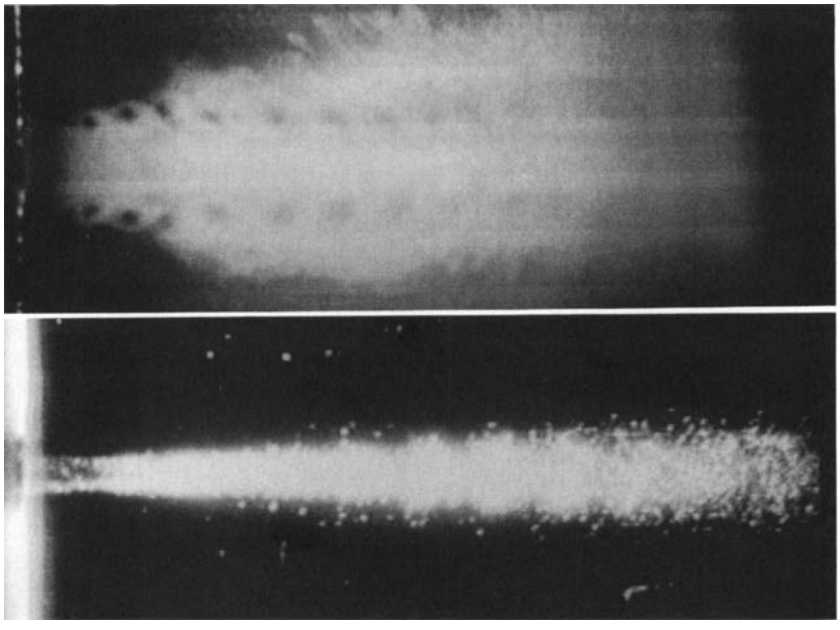

FIGURE 9. Single-phase and particle-laden flow, $St_D = 0.93$, $Re_D = 23000$.

curl back around the rings, the particles continue to move outward, hence the tails on the particle clusters. Between the clusters relatively few particles are observed, and in the regions of the vortex rings themselves, very few or no particles are observed.

Figures 8 and 9 exhibit images of flow forced at higher frequencies. We observe from the smoke-marked flow that the size of the vortex rings becomes progressively smaller. Near the jet exit, the rings in these figures are spaced more tightly. The rings appear to maintain the same core size and spacing as they move downstream through the extent of the laser sheet ($0 < x/D < 9$). The strobed images do not show evidence of systematic pairing in the jet near field. This result contradicts those of Bouchard & Reynolds (1982) who observed early pairing in a jet forced with a large-amplitude high-frequency wave so that vortex passage frequencies at $x/D = 4$ were always less than $St_D = 0.45$. Our only explanation for this contradiction is that the fundamental forcing was probably strong enough to delay any systematic pairing from occurring over the range studied.

As the forcing frequency is increased, the tendency of the particles to form distinct clusters is decreased. Although clusters are still evident at $St_D = 0.76$, they are more tightly spaced and less distinct than those seen at $St_D = 0.26$ and 0.43, and tails due to outward ejection of particles are not apparent. The particle-laden flow forced at $St_D = 0.93$ (see figure 9) does not contain distinct clusters, but the waviness seen on the outer edges of the particle stream provides evidence that the flow structures still influence particle motion.

Figure 10 depicts instantaneous views of forced flow from Jet 2 at $Re_D = 19000$ and $St_D = 0.51$. The exact forcing frequency and jet core fluctuation level are listed in table 2. Here, the flow was illuminated by a single laser pulse for each photograph. The phase is identical in each photo so the positions of particle clusters can be compared to the vortex-ring positions. The instantaneous view looks very similar to the visualization in figure 7 ($Re_D = 23000$, $St_D = 0.43$). In figure 10, the coherent

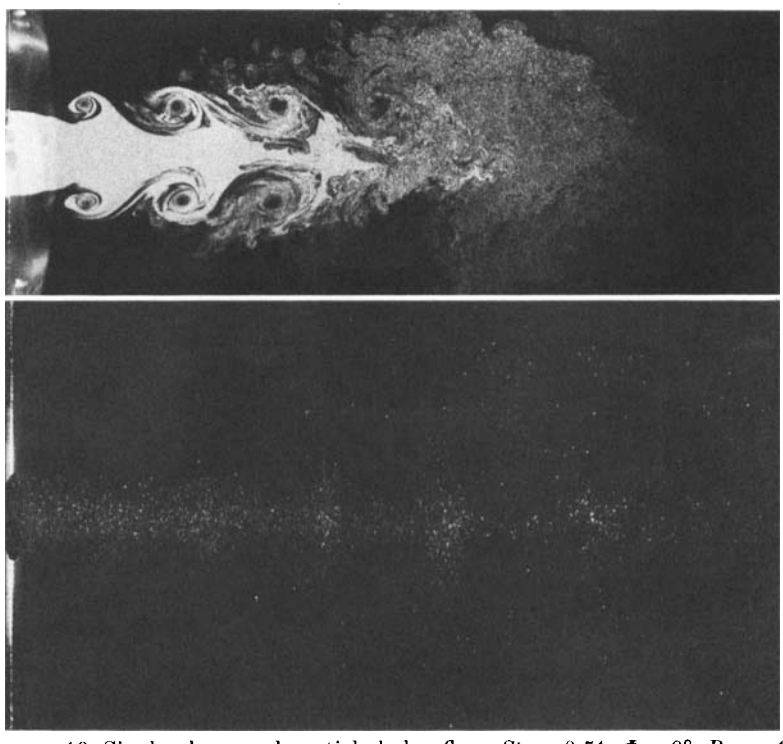

FIGURE 10. Single-phase and particle-laden flow, $St_D = 0.51$, $\Phi = 0°$, $Re_D = 19000$.

Frequency (Hz)	St_D	u'/U
364	0.51	0.11
648	0.90	0.045
362+181(0)	0.51+0.25	0.11

TABLE 2. Forcing amplitudes for Jet 2

vortex rings appear to break down before the downstream limit of the laser sheet. This discrepancy is most probably caused by the differences in the photographic technique. The superposition of several images (12 for $St_D = 0.43$) on the videotape causes differences in scattering intensity in a single image to be multiplied. Therefore, structures which may not stand out in a single image can become clear on the videotape. Although distinct structure is difficult to see beyond $x/D = 5.5$ in the smoke-marked image in figure 10, the effect of structure on the particles is visible up to $x/D = 8$. As we saw for the strobed low-frequency cases in figures 6 and 7, the photograph of particle-laden flow in figure 10 shows heavier concentrations of particles in the regions between neighbouring vortex rings. Very few or no particles appear in the ring core regions, and tails occur on the particle clusters where particles are thrown outward from the jet axis. Particle dispersion by diffusion is not a dominant mechanism as local concentration of particles located far from the jet axis is sometimes greater than concentration nearer the jet axis.

Flow forced at a higher frequency ($St_D = 0.90$) is displayed in figure 11. As with the strobed visualization in figure 9, smaller, more closely spaced vortices are present. No strong clustering occurs in the particle-laden flow, but some periodic waviness

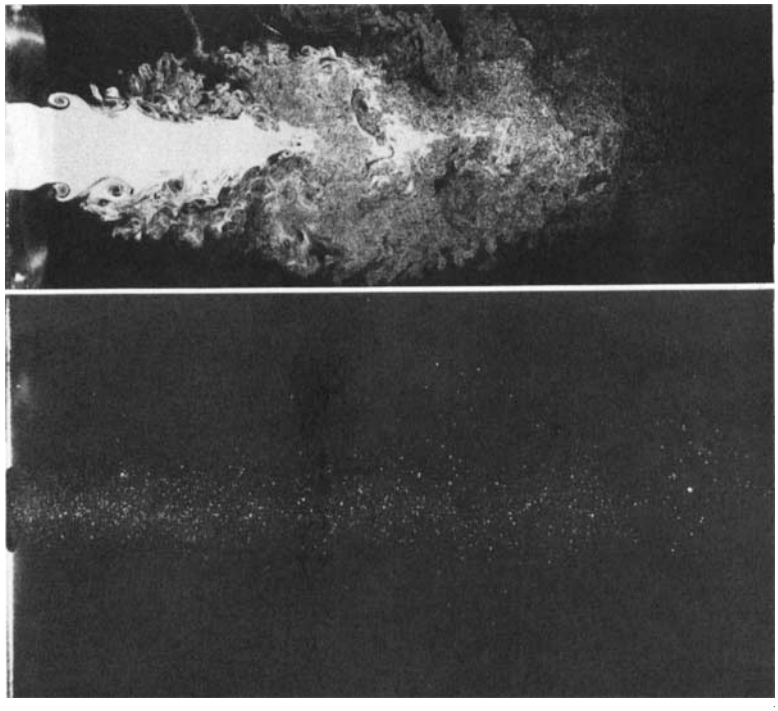

FIGURE 11. Single-phase and particle-laden flow, $St_D = 0.90$, $\Phi = 0°$, $Re_D = 19000$.

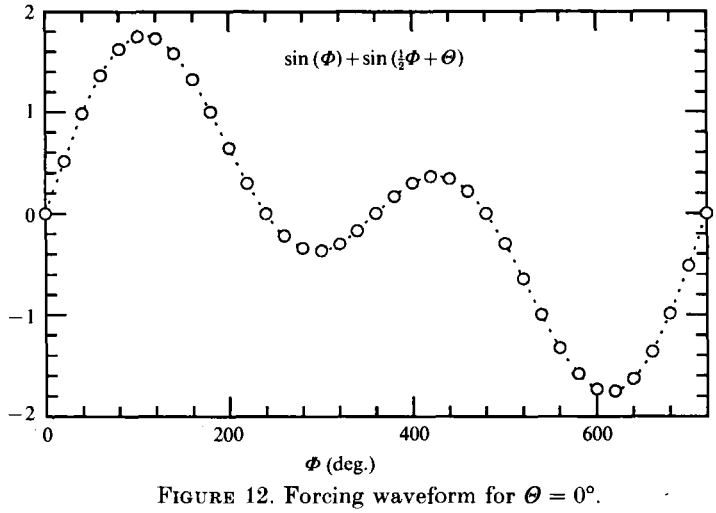

FIGURE 12. Forcing waveform for $\Theta = 0°$.

appears in the radial extent of the particle distribution between $x/D = 1$ and $x/D = 3$. It is not clear whether particles are flung away from the jet axis as occurred for $St_D = 0.51$.

To examine the effect of vortex pairing on particle movement, the flow was forced with two frequencies simultaneously: a fundamental plus its first subharmonic. The amplitudes of the two waves were equal, and the relative phase (Θ) at which the two waves were summed was set at 0°. The forcing waveform is plotted in figure 12. This forcing strategy caused sets of neighbouring vortex rings to pair at a fixed axial location into larger, stronger vortices.

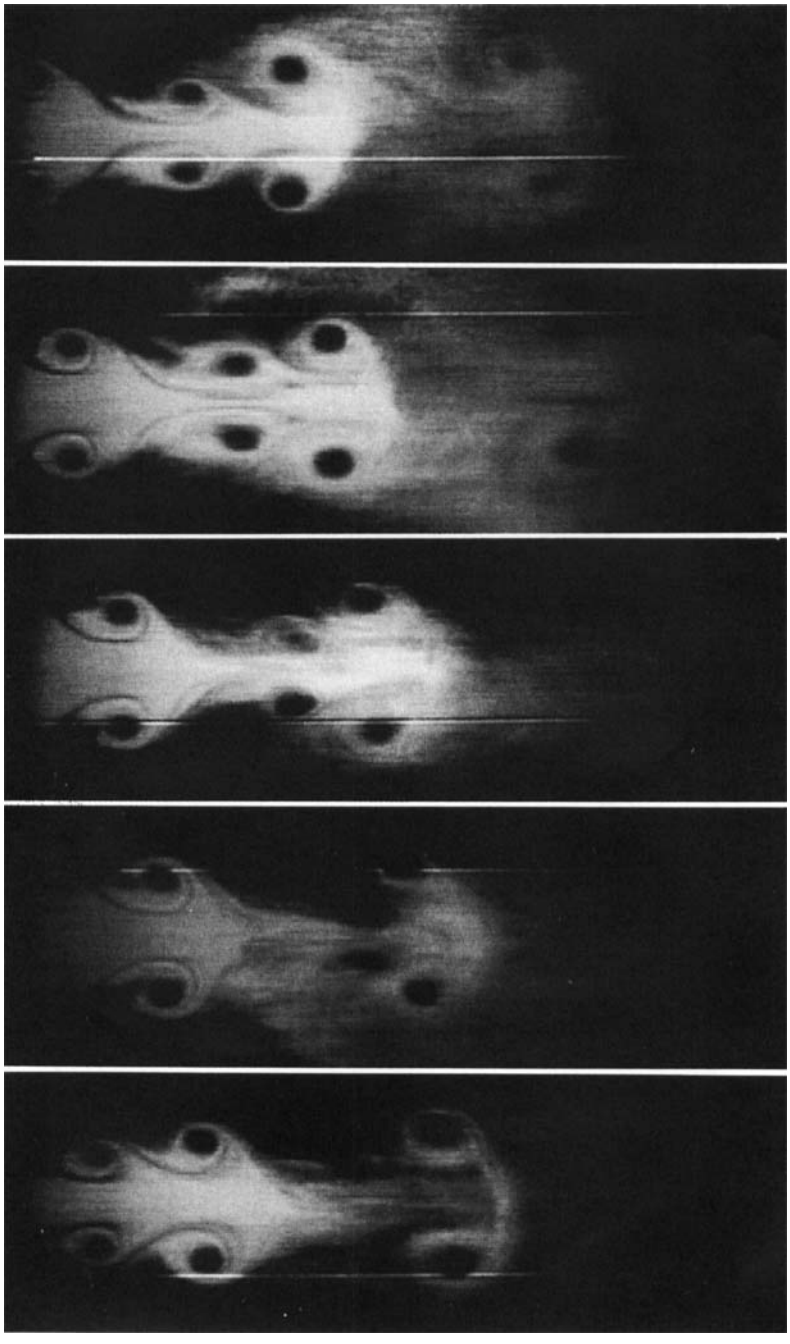

FIGURE 13. Single-phase flow, $St_D = 0.43 + 0.215$, $\Theta = 0°$, $Re_D = 23000$.

Figure 13 exhibits strobed visualization of single-phase flow for the case of $Re_D = 23000$, $St_D = 0.43 + 0.21$. Since the laser was strobed at the subharmonic frequency (181 Hz), each photograph contains a superposition of 6 flow images. The photographs illustrate the nature and location of the pairing process. Figure 14 displays strobed images of particle-laden flow forced under the same conditions. In

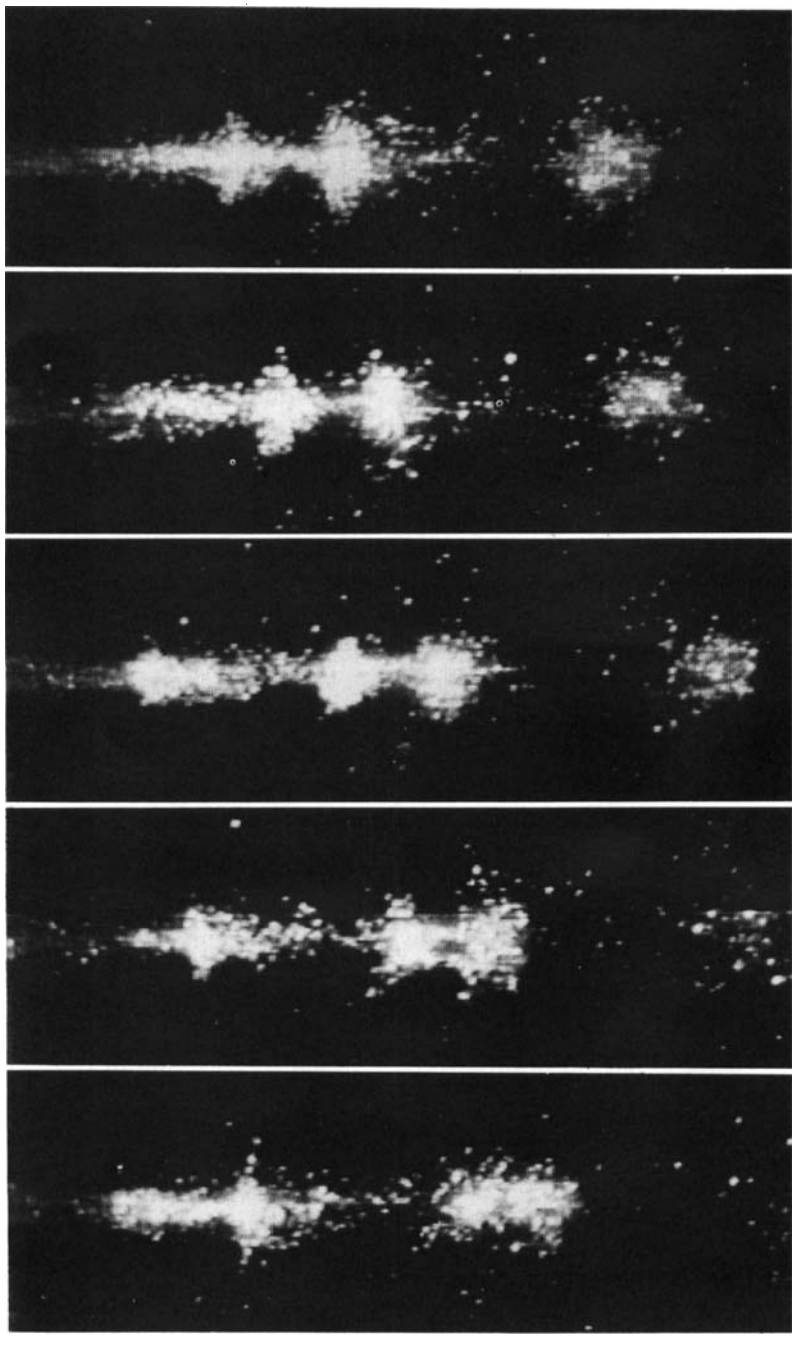

FIGURE 14. Particle-laden flow, $St_D = 0.43+0.215$, $\Theta = 0°$, $Re_D = 23000$.

this sequence, pairs of particle clusters form and merge just downstream of the axial location where the vortex rings pair. A larger 'paired' cluster displays 'tails' where particles are convected away from the jet centreline.

Videotapes of smoke-marked, particle-laden flow were examined in an attempt to understand the cluster pairing process and the relatively rapid dispersal of particles

after pairing. Prior to pairing, each particle cluster moves with the velocity of its respective vortex ring. Thus, the particles near the centre of each cluster (where particle concentration is high) are approximately in dynamic equilibrium with the flow. The upstream ring moves faster than the downstream ring and carries its particle cluster towards the downstream cluster. As the rings approach pairing, the upstream ring accelerates, and the downstream ring decelerates. The actual pairing of the vortex rings is very violent: the upstream ring accelerates into the downstream ring, then decelerates and wraps around it forming a single larger ring. At this point, the two clusters appear to merge. At least two factors act to rapidly disperse the merged cluster. First, the particles from the upstream cluster cannot decelerate as rapidly as the fluid so move on ahead of the merged cluster leaving the slower moving particles of the downstream cluster behind. The time history of particle acceleration here is probably highly dependent on the particles' initial radial position prior to the pairing. This effect spreads the merged cluster in the axial direction. The second factor acting to disperse the particles more rapidly is the longer timescale of the 'paired' ring. The larger ring becomes more effective at spreading particles radially. This effect would not occur suddenly, but must certainly have a significant impact over the distances examined in the experiment.

4.2.2. *Particle number density measurements*

To obtain a quantitative assessment of the particle distributions in the single and double frequency forced cases, particle number density maps were computed by counting all of the particles in sets of 25 photographs for each case. (Figures 10 and 11 contain samples of these photographs.) The resulting contour maps were normalized by the total number of particles counted so that variations in the mass loading ratio for the different cases would not influence the results. The lowest contour level in each map represents a grid point value of 0.0002, and each succeeding level is incremented by 0.0004. The minimum contour level corresponds to 9 particles counted at a single grid point for a case where about 45000 particles were counted in total. For the cases shown, the maximum normalized particle density at a given grid point varied between 0.0035 and 0.0046 representing maximum numbers of particles per grid point of 130–250.

Figure 15 shows number density maps for the cases $St_D = 0.51$ and $St_D = 0.90$. The first point to notice is that in both plots, the radial distribution of particles exiting the nozzle is not uniform. Rather the particles are heavily concentrated near the centre of the nozzle exit. Away from the jet centreline, the contours near $x = 0$ are spaced fairly evenly, suggesting a linear decrease in local number density with increasing r. In the plot of $St_D = 0.90$, the particle number density decreases monotonically with increasing axial distance from the nozzle exit. Some effects on the particle dispersion pattern from the phase-locked vortex ring structures can be seen. The outer contour lines oscillate back and forth in the region between $x/D = 1$ and 4. The bulges in the contour lines are spaced at distances of approximately $0.7D$. This spacing yields a cluster (or bulge) propagation velocity of about 9.1 m/s.

For $St_D = 0.51$, the radial spread of the contours at the jet exit is approximately the same as that for $St_D = 0.90$. Just as the instantaneous photograph of the phase-locked flow showed (figure 10), strong clustering of the particles occurs between vortex ring structures. Along the jet axis, the local number density does not decrease monotonically with increasing x. Instead it alternately increases and decreases according to the locations of the clusters. For example, the two clusters centred at

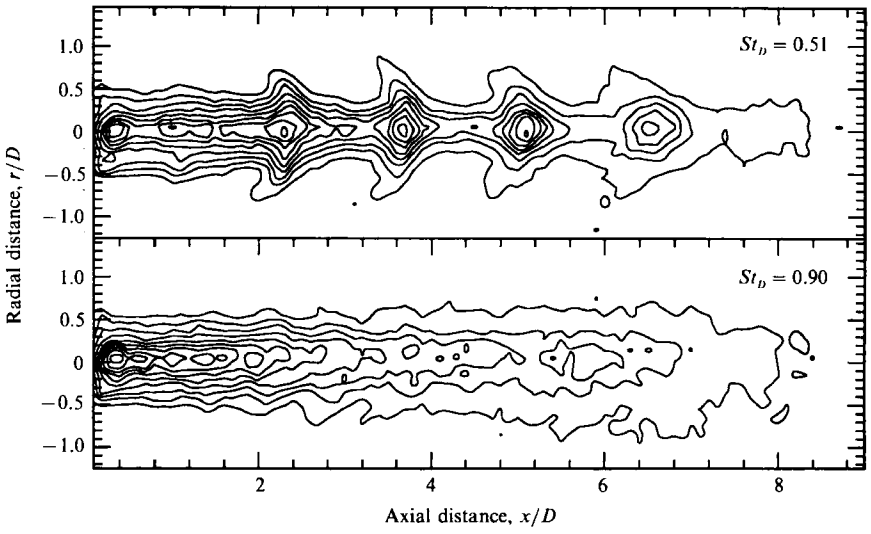

FIGURE 15. Particle number density maps, $St_D = 0.51, 0.90$.

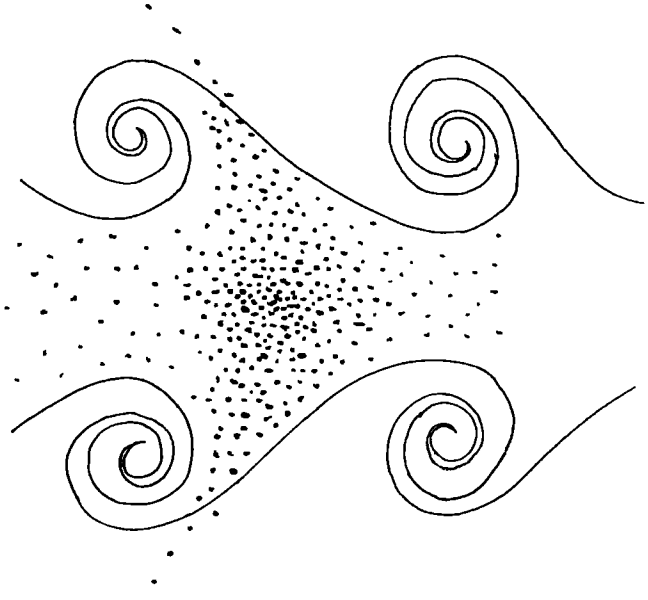

FIGURE 16. Cartoon of particles interacting with vortex ring.

$x/D = 2.2$ and 3.6 have peak normalized number densities above 0.0034 and 0.0030 respectively. These values are almost twice as high as the local number density along the jet axis halfway between the clusters which drops below 0.0018. Also, the radial spread of the contours at the axial positions of the two clusters is over twice as large as the minimum spread between the clusters. These results suggest that particles are pulled out of the streaming regions inside the vortex rings (near $r = 0$) and pushed into the regions downstream of the cores where the clusters appear. This concept is illustrated in figure 16.

We observe from the contour plot that the clusters begin forming at $x/D = 1$ and maintain approximately the same shape and spacing until $x/D = 6.5$. Then the

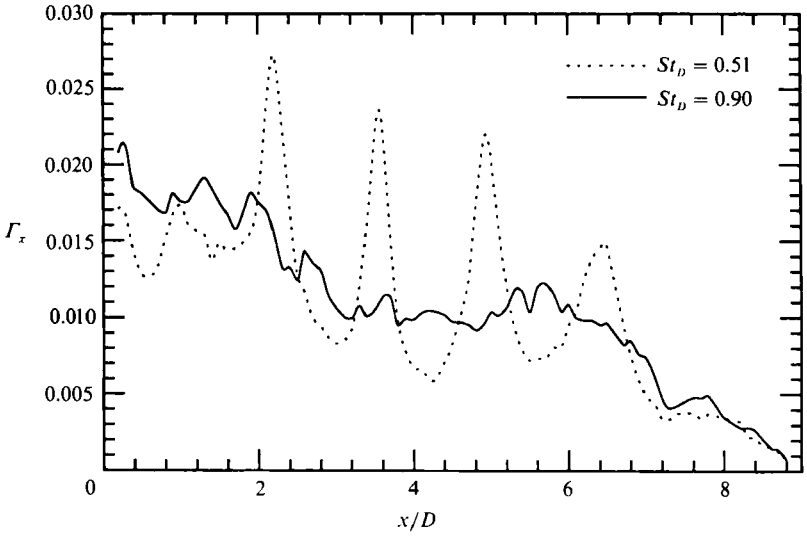

FIGURE 17. Γ_x *vs.* x/D, $St_D = 0.51, 0.90$.

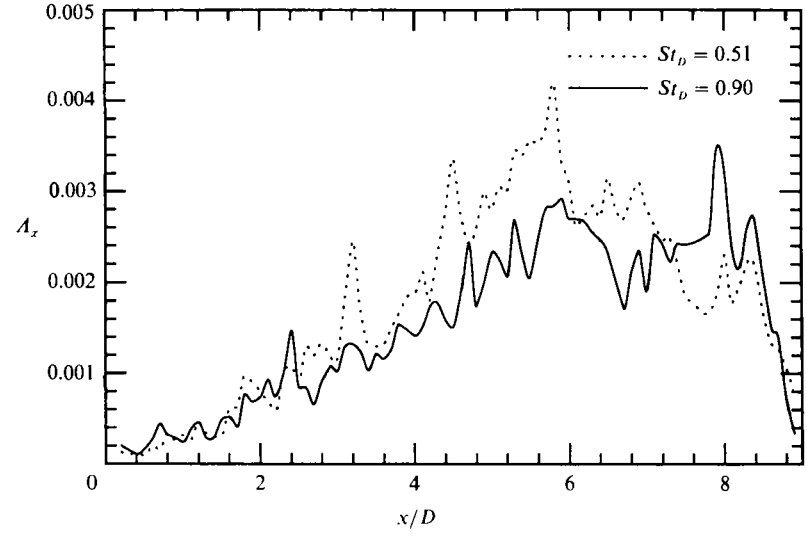

FIGURE 18. Λ_x *vs.* x/D, $St_D = 0.51, 0.90$.

clusters become rounder, and the tails disappear. The spacing between clusters is about $1.45D$ yielding a cluster propagation velocity of 10.5 m/s. The local number density in the centres of the clusters decreases gradually with increasing axial distance as the particles are convected outward continuously in the saddle regions. Also, the contours show that the vortex core regions contain very few particles.

Figures 17 and 18 provide further information about the number density maps. In figure 17, the function Γ_x is plotted, where Γ_x represents the integral over r of the normalized particle number density at a given x position. In both cases Γ_x decreases in general as x increases. For $St_D = 0.90$, the plot of Γ_x oscillates in the region between $x/D = 1$ and 3 just as the contour lines in figure 15 oscillated. The spacing

between peaks in the curve is again about $0.7D$. The axial positions of the peaks are located slightly upstream ($\sim 0.1D$) of the contour line 'bulges' discussed in the previous paragraph.

For $St_D = 0.51$, sharp peaks occur in Γ_x slightly upstream of the axial locations of the particle cluster centres (i.e. the positions of peak number density). These peaks reach values that are greater than the value measured at the nozzle exit again suggesting that particles are displaced axially *into* the clusters (rather than that particles are merely dispersed from the low density regions near the jet centreline while remaining in the same axial plane). The absolute values of the peaks in Γ_x are more than three times as high as the values in the valleys. Thus, when we integrate across r, the axial variation in particle number density appears even stronger than when we observe the variation along the centreline only. As one would expect from observing the contour plots, the spacing between peaks in Γ_x (about $1.4D$) remains constant from $x/D = 1.5$ to $x/D = 6.5$. No peaks are found downstream of $x/D = 7$ implying that the particle clusters have dispersed. (The intensity of the laser sheet was reasonably constant up to $x/D = 8$, but decreased beyond this point.)

Figure 18 shows Λ_x which represents the sum of normalized particle densities outlying the lowest contour level (0.0002) at a given x position. This function was plotted to determine the relative number of particles which have moved away from the main particle stream, i.e. the number of particles in sparsely populated areas. The plots in the figure appear fairly noisy, but do have three interesting features. First, the level of Λ_x is consistently higher for $St_D = 0.541$ than it is for $St_D = 0.90$. The total area under the curve for $St_D = 0.51$ is 20% greater than the area computed for $St_D = 0.90$. Therefore, the percentage of particles in sparsely populated regions of the field of view is greater for flow containing larger vortex rings. The second point to notice is that distinct peaks occur in the plot of Λ_x for $St_D = 0.51$. These peaks, which are spaced at about $1.35D$, must correspond to regions where particles have been propelled away from the jet axis by the outwardly moving flow on the downstream edges of the vortex ring cores (refer to figures 7 and 10). The peaks in Λ_x occur about $0.4D$ upstream of the peaks in Γ_x and the particle cluster centres which is consistent with the idea that the outlying particles lag the particles near the jet centreline.

The third remarkable feature of the plots in figure 18 is their overall shape. For $St_D = 0.51$, the value of Λ_x increases with x until $x/D = 6$ where it levels off and begins to decrease. The behaviour of Λ_x for $St_D = 0.90$ is less clear, but the curve appears to increase or at least not decrease until $x/D = 8$. One explanation for the earlier decrease in Λ_x for $St_D = 0.51$ is that by $x/D = 6$, a significant number of particles have travelled far enough in the radial direction ($r/D \sim 3$) to pass out of the camera field of view (see figure 10). The number of particles being propelled away from the jet centreline (which is decreasing with x since the local centreline density decreases with x) is fewer than the number of particles leaving the field of view.

Particle number density maps were computed for a double frequency case with conditions $St_D = 0.51 + 0.25, \Theta = 0°$. Contour plots of the maps for four phases of the forcing cycle are plotted in figure 19. In this series of plots, it can be observed that two distinct particle clusters have formed at $x/D = 1.8$ and $x/D = 2.9$. The spacing between clusters is $1.1D$ which is slightly smaller than the spacing between neighbouring clusters in the $St_D = 0.51$ single frequency case (see figure 15). The clusters in figure 19 appear somewhat less distinct than those occurring for $St_D = 0.51$. The variation in the radial spread of the contours over x in the vicinity of the clusters is smaller, and the tails on the particle clusters for $x/D < 4$ are less distinct than those in figure 15.

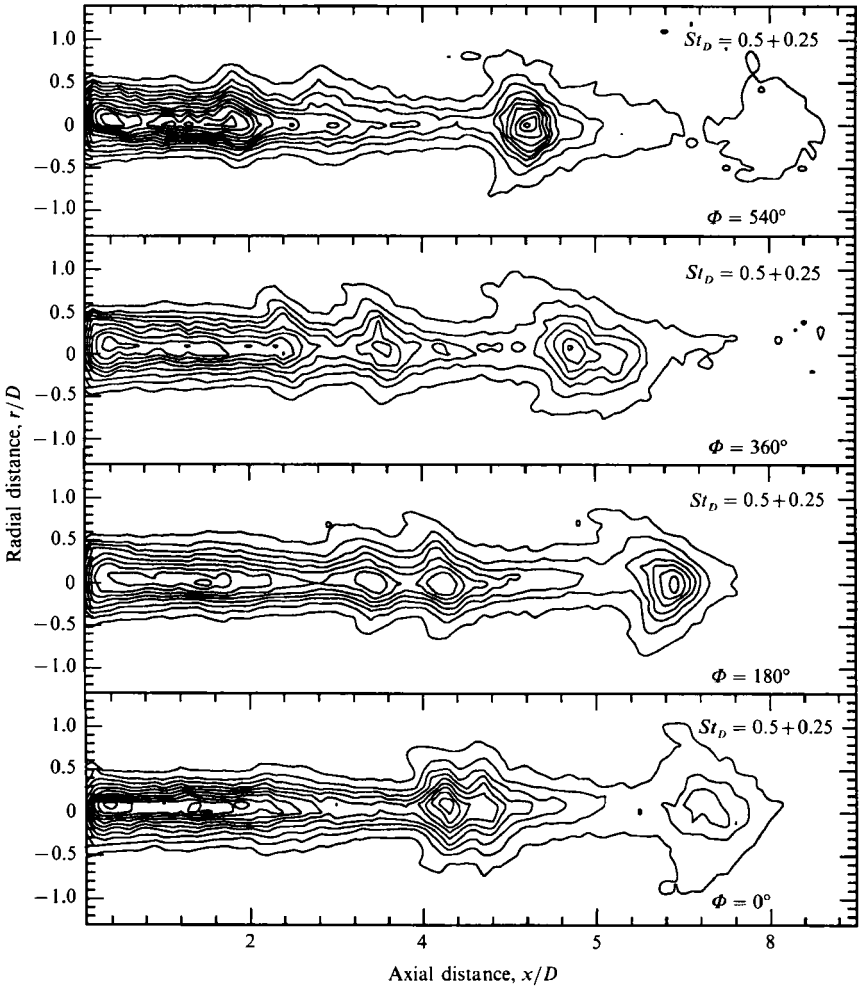

FIGURE 19. Particle number density maps, $St_D = 0.51+0.25$.

The spacing between the two clusters in the double frequency case decreases with increasing x until the clusters merge at $x/D = 5$ which is slightly downstream of the vortex pairing position determined from instantaneous photographs of smoke-marked flow. At $x/D = 5$, the peak number density has increased to 0.0038. Therefore, the particles have become more concentrated as they have moved downstream in the jet and the two clusters have paired into one. The 'paired' cluster is larger than the clusters occurring for $St_D = 0.51$ and the unpaired clusters upstream in figure 19, i.e. the total area covered by contours in the paired cluster is greater. The paired cluster shown in the plot of $\Phi = 540°$ also has strong tails indicative of particle ejection at this location. The spread of contours just upstream of this cluster is reduced from the spread near the nozzle exit indicating a local paucity of particles. The contours show that at this location the centreline number density increases from 0.0010 to 0.0038 (an increase of 380 %) over an axial distance of only $0.5D$. Hence the spatial variation in local number density is not gradual, but rather quite radical.

The shape of the paired cluster remains approximately constant, and the peak number density decreases as it moves downstream to $x/D = 7$. The tails on the

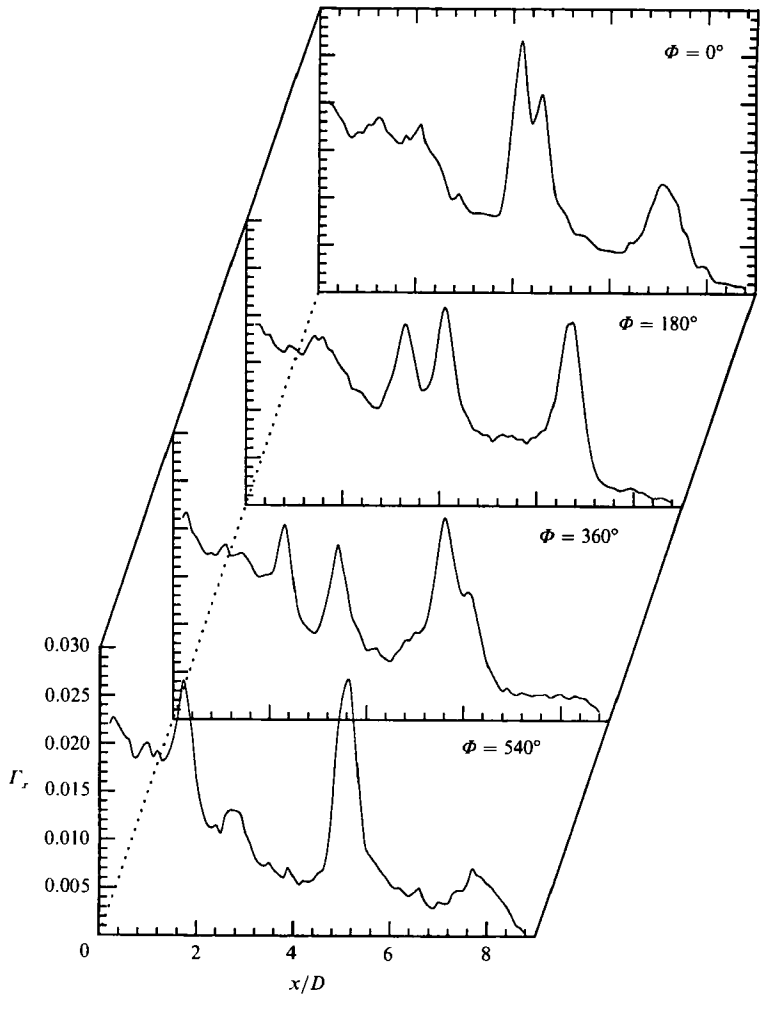

FIGURE 20. Γ_x *vs.* x/D, $St_D = 0.51 + 0.25$.

cluster remain indicating that particles continue to be ejected from the cluster over this axial range. Between $x/D = 7$ and $x/D = 7.3$, the peak number density in the cluster drops suddenly from 0.0026 to 0.0010. This implies that between these axial locations, strong dispersion of the particles occurs.

Figure 20 shows plots of Γ_x for the four different forcing phases of the $\Theta = 0°$ case. The peaks in Γ_x for the different forcing phases correspond very well with the centres of the particle clusters found in figure 19. For example, the strong peak at $x/D = 5.1$ in $\Phi = 540°$ corresponds to the strong, dense cluster in figure 19. For x/D aligned with the centre of this peak, the value of Γ_x is about five times as large as Γ_x on either side of the peak. Thus, we see again that this cluster is stronger than the clusters in the $St_D = 0.51$ forcing case (compare with figure 16).

Figure 21 displays a plot of Λ_x for the double frequency forcing case. In general, these plots appear noisy, and evidence of structure is difficult to find. The plots for $\Phi = 0°$, 180°, and 540° all show peaks in Λ_x at axial positions approximately $0.3D$ upstream of the tails of the paired cluster. A similar peak in Λ_x for $\Phi = 360°$ could not be found, perhaps because the outer contour on the upstream end of the paired

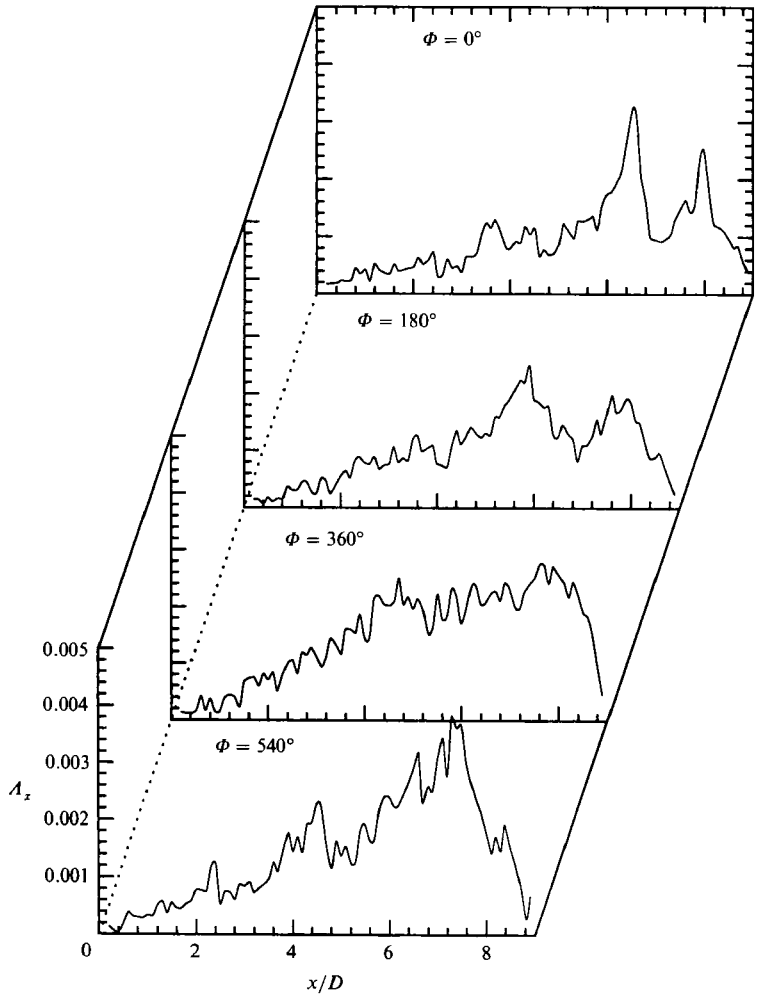

FIGURE 21. A_x *vs.* x/D, $St_D = 0.51 + 0.25$.

cluster for $\Phi = 180°$ extends relatively far beyond the next highest contour. At any rate, the three peaks mentioned above provide evidence that particles are being flung outward from the large paired cluster. Also, the axial positions of greater concentrations of outlying particles, i.e. particles in sparsely populated regions, are dependent on structures in the jet.

When A_x is summed over x for all four cases, the average value obtained is 0.11, which is less than the values obtained for single-frequency forced flow (0.14 and 0.17). The results imply then that over the axial range of x/D from 0 to 8, fewer particles are ejected from the jet inner region in flow forced with subharmonics than in flow forced with a single frequency.

4.2.3. *Particle velocity measurements*

In order to determine not only where particles were located in relation to flow structures, but also how fast they were moving, detailed velocity measurements were obtained for the $St_D = 0.51$ forcing case. Results from time-averaged particle velocity measurements in Jet 2 are plotted in figures 22–24. The mean fluid velocity at the

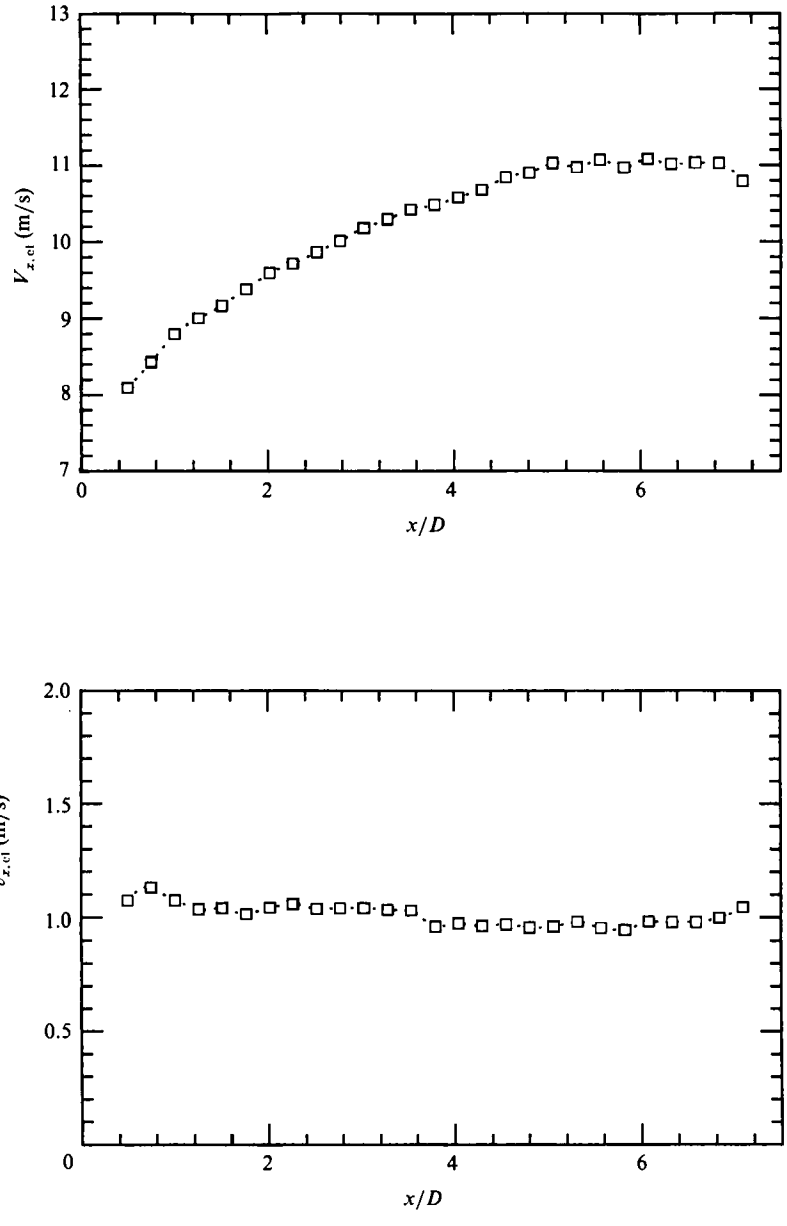

FIGURE 22. Time-averaged particle centreline velocity: (*a*) mean, (*b*) standard deviation.

nozzle exit was 14.4 m/s in all cases (corresponding to $Re_D = 19000$). Figure 22 shows the axial variation of particle centreline velocity. The mean particle velocity at the nozzle exit is about 8 m/s, and the velocity increases with downstream distance. Although the fluid accelerates through the nozzle because of the area contraction, the particles accelerate because of viscous interaction with the fluid. Therefore they lag the fluid and continue to accelerate downstream of the nozzle exit where the fluid must actually decelerate on average. The mean centreline velocity of the particles levels off at about 11 m/s at a position of $x/D = 5$. The standard deviation of the particle centreline velocity is plotted in figure 22(*b*). The absolute standard deviation

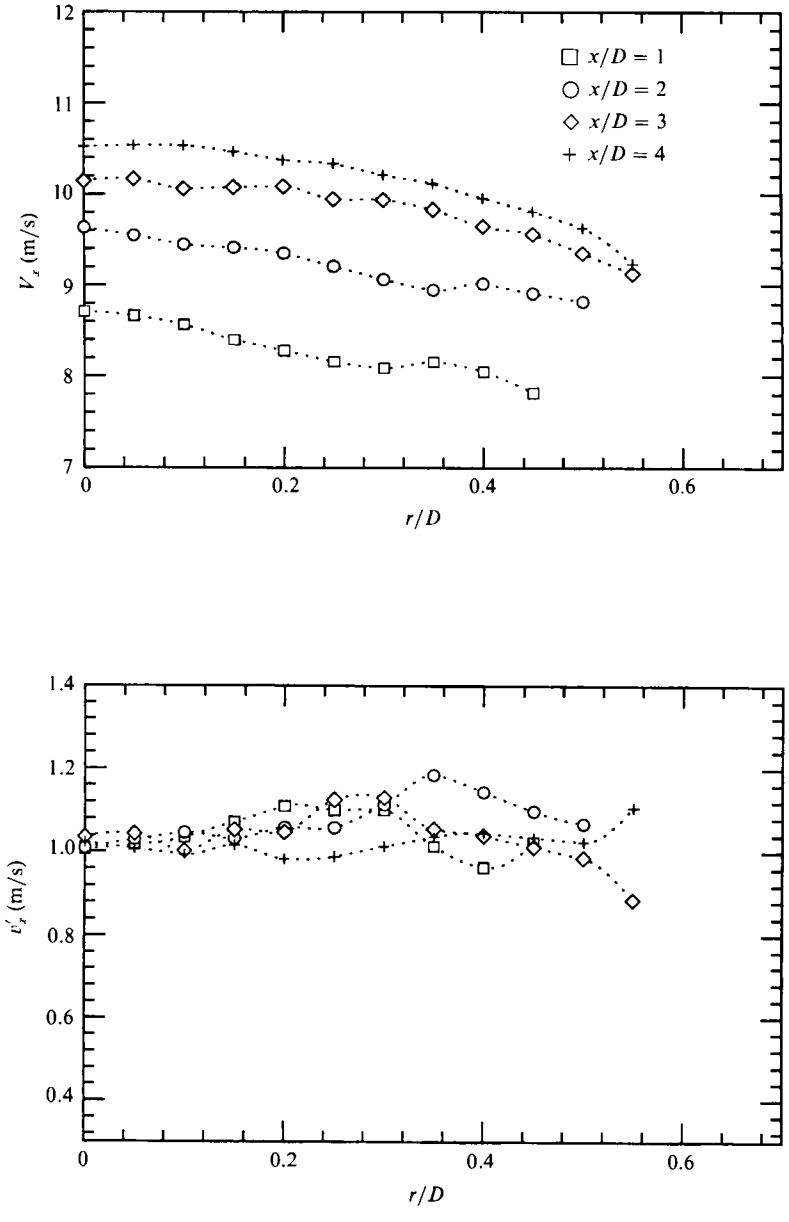

FIGURE 23. Time-averaged particle axial velocity: (*a*) mean, (*b*) standard deviation.

in particle velocity remained approximately constant as one moved downstream in the jet meaning that the relative standard deviation (v'_x/V_x) decreased.

Figure 23 exhibits plots of time-averaged velocity profiles of V_x and v'_x at four axial positions: $x/D = 1$, 2, 3 and 4. The profiles are relatively flat out to the radii where significant numbers of particles could be counted. (Profiles were cut off when the data rate dropped below 20 counts per second. See §3.3.) The outer limits of the radial profiles did not increase significantly beyond the nozzle radius up to $x/D = 4$ indicating that a large percentage of the particles remained tightly collimated over this axial distance.

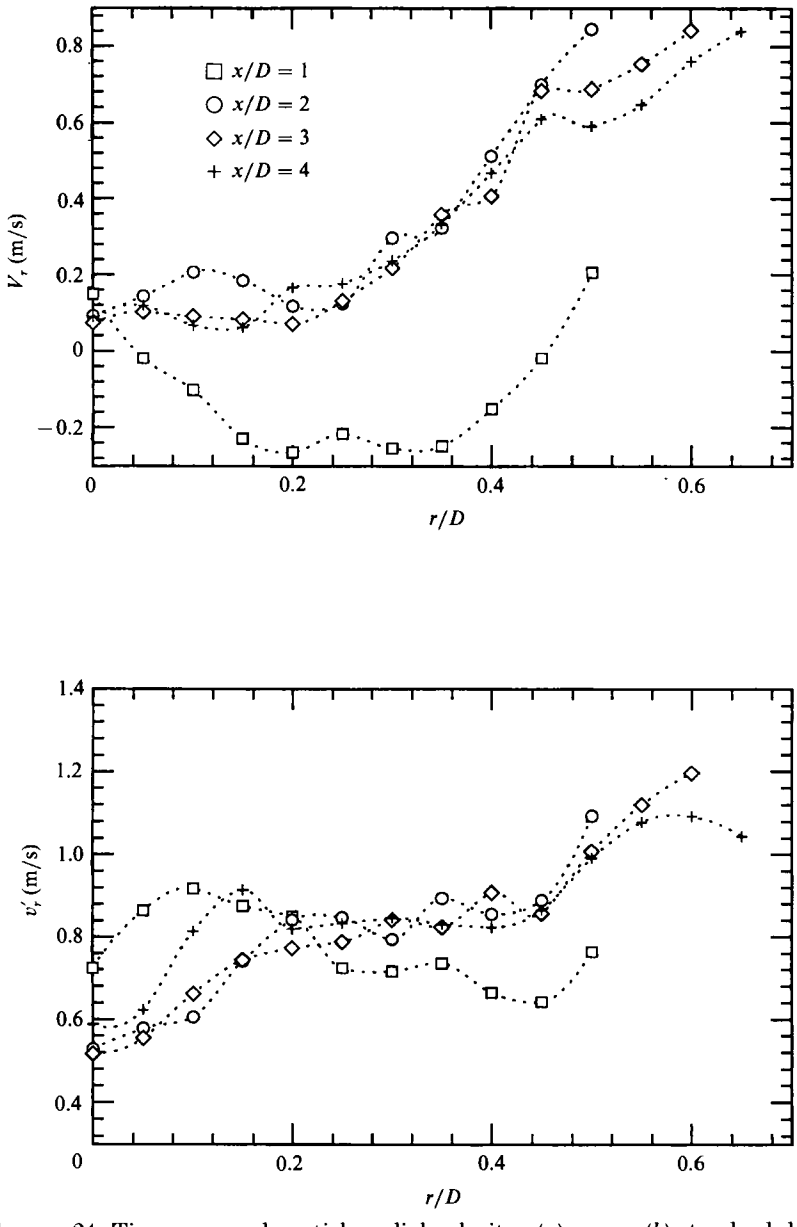

FIGURE 24. Time-averaged particle radial velocity: (*a*) mean, (*b*) standard deviation.

Time-averaged profiles of radial particle velocities are displayed in figure 24 for the axial positions $x/D = 1$, 2, 3 and 4. At $x/D = 1$, the profile of mean radial velocity indicates that over most of the radial range, particles are moving toward the jet axis. Most probably this results from particles gaining negative radial velocities as they flow through the first half of the jet nozzle. Although the air flow straightens out through the second half of the contraction, the particles have too much inertia and continue to flow inward. At later axial positions ($x/D = 2$, 3 and 4), the mean radial particle velocities become positive. The shapes of the mean profiles are similar from $x/D = 2$ to 4 except that for $r/D > 0.4$, V_r decreases with increasing axial distance.

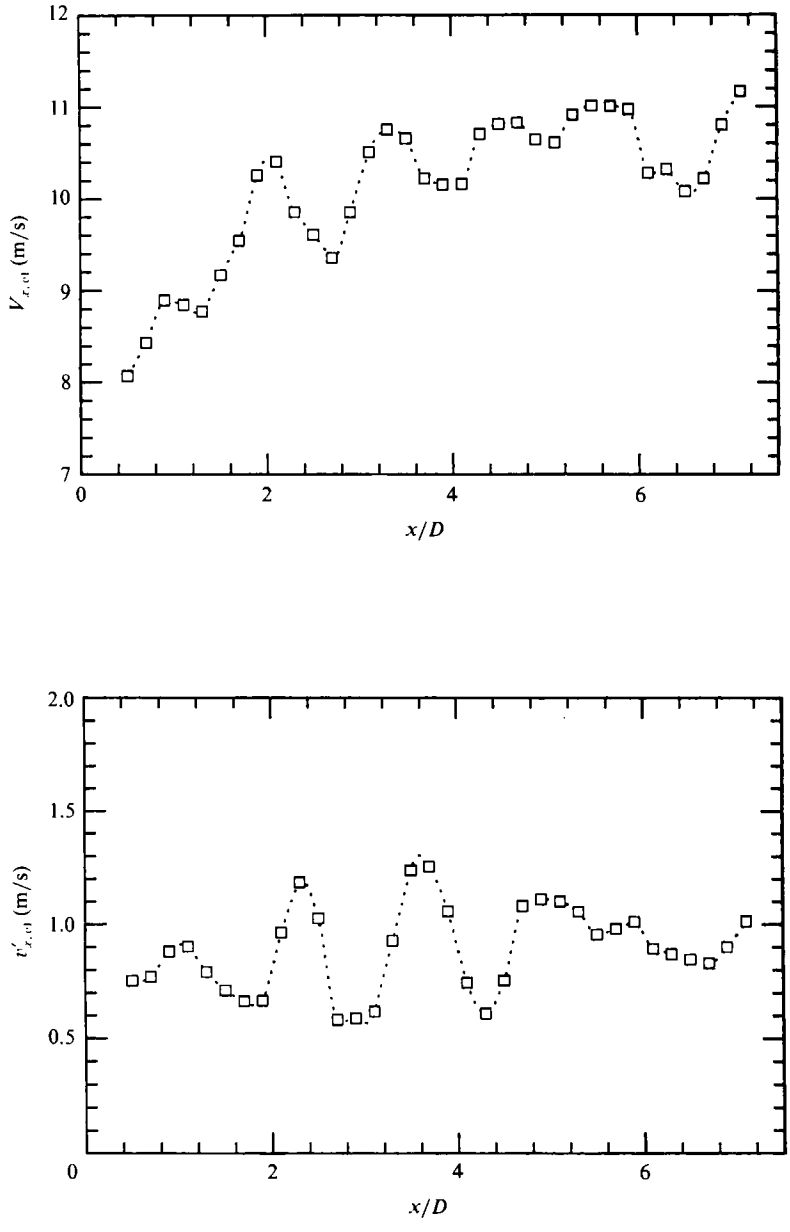

FIGURE 25. Phase-averaged particle centreline velocity, $\Phi = 0°$: (*a*) mean, (*b*) standard deviation.

It is difficult to distinguish meaningful trends in the behaviour of the standard deviations in radial velocity over the distance $x/D = 1$–4. Note, however, that for $x/D = 2$–4 and $r/D > 0.2$, v'_r is higher than at $x/D = 1$.

Results from phase-averaged particle velocity measurements are presented in figures 25–28. All velocity measurements were obtained from a 15° bin centred on $\Phi = 0°$. Figure 25 displays the axial variation in mean and r.m.s. particle centreline velocity. The plot of $V_{x,cl}$ in figure 25 (*a*) shows the same overall trend as the plot in figure 22 (*a*) (time-averaged particle centreline velocity). In general, $V_{x,cl}$ is much lower than U_x near the jet nozzle exit and increases with increasing x up to

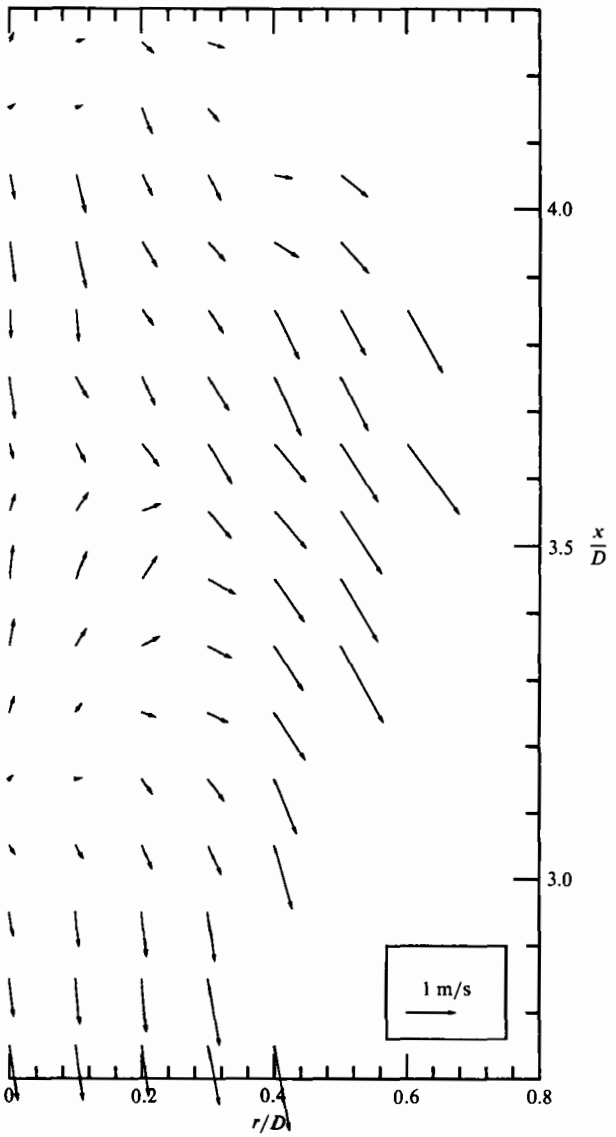

FIGURE 26. Phase-averaged particle velocity vectors, $\Phi = 0°$.

$x/D = 5.5$. The phase-averaged plot, however, shows periodic fluctuations in the mean particle velocity which are not seen in the time-averaged plots. The spacing between the peaks of the oscillations is about $1.3D$. Thus, particle velocities become correlated with the local flow structures. The particle velocity peaks occur *upstream* of the particle clusters, where the local particle velocity is greater than the local cluster convection velocity. Conversely, the local minima in the particle centreline velocity occur *downstream* of the particle clusters. The plot of $v'_{x,\mathrm{cl}}$ in figure 25(*b*) shows oscillations at the same frequency as those in figure 25(*a*). Note that the peaks in $v'_{x,\mathrm{cl}}$ do not occur at the same axial locations as the peaks in $V_{x,\mathrm{cl}}$. The peaks in $v'_{x,\mathrm{cl}}$ occur approximately at the midpoints of the downward sloping sides of the oscillations in $V_{x,\mathrm{cl}}$ which also coincide with the peaks in Γ_x seen in figure 20. Thus, maxima in the r.m.s. particle centreline velocity occur in the regions of high strain

which are aligned approximately with the centres of the particle clusters, and where the fluid is decelerating in the axial direction. The minima in $v'_{x,\mathrm{cl}}$ occur in the streaming regions inside of the vortex ring cores where the fluid is accelerating.

Figure 26 shows a plot of particle velocity vectors for $\Phi = 0°$. Vectors were plotted for $2.7 < x/D < 4.3$ at all radial positions where the LDA sampling rate was sufficiently high for both V_x and V_r (see §3.3). The variation in the number of vectors plotted at each axial location is then a result of the variations in particle number density over x and r that were shown in figure 15. The particle cluster convection velocity of 10.5 m/s as calculated from the local cluster spacing in figure 15 was subtracted from the total velocity at each point so that we are examining a reference frame which moves with the clusters. The tails of the arrows in the plot are positioned at the points where the velocity magnitude and direction were calculated. The vector lengths are scaled so that the longest vector in the plot (at $x/D = 3.35$, $r/D = 0.5$) represents a velocity magnitude of 1.51 m/s. From figure 25(*a*), it can be seen that the axial distance covered by figure 26 contains both a maximum and a minimum in $V_{x,\mathrm{cl}}$. Furthermore, this region contains a maximum and a minimum in $v'_{x,\mathrm{cl}}$ (see figure 25*b*). We also observe from figure 25(*a*) that when the cluster convection velocity is subtracted from the particle centreline velocity in this region, both positive and negative values of V_x will occur.

Looking at figure 26, we see two particle 'source' regions and a particle 'stagnation' region centred on the jet axis at $x/D = 3.05$, 4.10 and 3.65.'Source' regions are possible since the flow of particles is time dependent. Thus, more particles can leave a given control volume than enter it. In the source regions, the particle axial velocities are accelerating as x increases, and in the stagnation region they are decelerating as x increases. The source and stagnation regions occur where $v'_{x,\mathrm{cl}}$ is a local minimum and maximum respectively (refer to figure 25*b*). As r increases above zero, the axial components of the velocity vectors generally follow the same trend as $V_{x,\mathrm{cl}}$. The level of V_x decreases with increasing r except in the region above the stagnation point. There, for small r/D, V_x actually increases above its centreline value. Farther away from the jet axis ($r/D > 0.3$) where the air flow is generally slower, all of the vectors (with one exception) are directed vertically downward implying that the mean particle velocities are all less than the cluster convection velocity.

Vectors of the radial velocity component alone are presented in figure 27. We observe from this plot that V_r is greater in the vicinity of the particle stagnation region than in the two source regions. For example, at $r/D = 0.3$, the radial velocity at $x/D = 3.45$ is four times higher than the radial velocity at $x/D = 2.95$. Also, we see that V_r typically increases as r increases, and the rate of increase is larger in the stagnation region. Thus, particles accelerate as they move away from the jet centreline with the rate of acceleration the strongest between x/D of 3.35 and 3.65. Note that we do not see any vectors directed toward the jet centreline. Hence particles are not moving toward the jet axis anywhere within the plotted field.

In figure 28, particle velocity has been multiplied by the local value of normalized particle number density to obtain the particle number flux. Therefore, areas of high particle concentration are emphasized. The longest vectors, and the vectors with the largest radial components are all located near $x/D = 3.55$. Recall from figures 15 and 16 that a particle cluster and a peak in Γ_x are centred at $x/D = 3.6$. In contrast, local minima in Γ_x occurred at $x/D = 3.0$ and 4.2 where, in figure 28, the number flux vectors are generally short with a very small radial component.

This plot helps explain two important concepts. First, particle clusters form

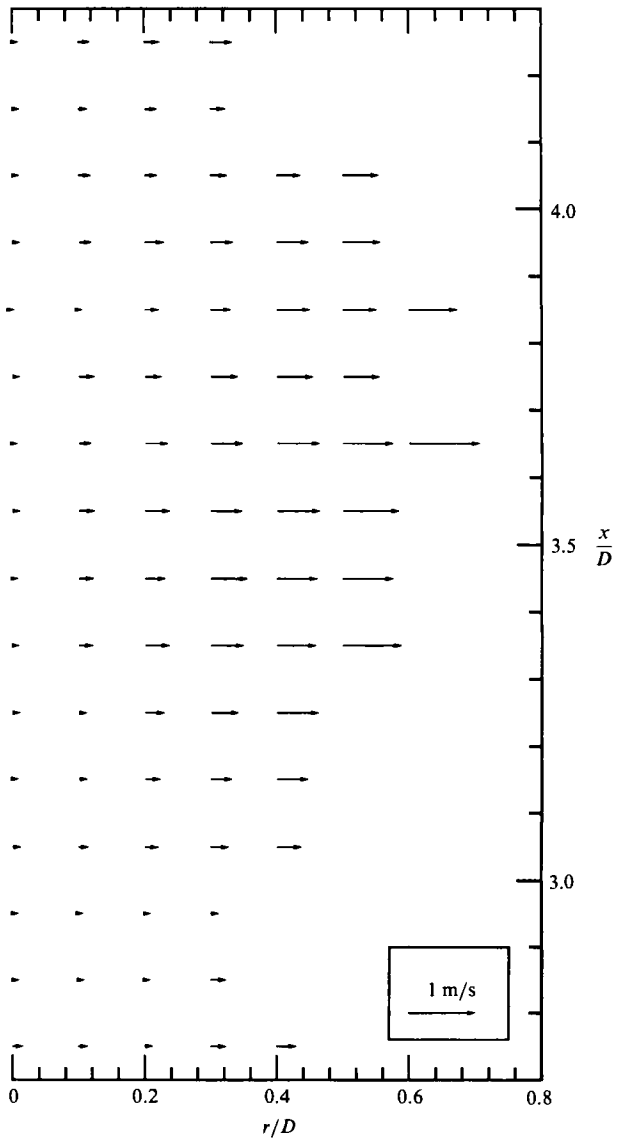

FIGURE 27. Phase-averaged particle radial velocity vectors, $\Phi = 0°$.

because particles are dragged into distinct axial regions from both upstream and downstream locations owing to local variations in the continuous fluid velocity. In figure 28, the centre of one of these regions occurs at x/D of about 3.6. Secondly, particles tend to disperse from the jet at specific axial locations. They do not disperse by diffusing away from areas of high concentration. Most particles are accelerated in the radial direction and propelled outward from the clusters described above which have been shown to occur downstream of large ring vortices. This process dominates any diffusive-type dispersion occurring elsewhere in the jet, e.g. near $x/D = 3.0$ in figure 28. The convective mechanisms apparent here would be masked completely by a time-averaged plot of the number flux which would yield vectors with much less local variation in length and direction.

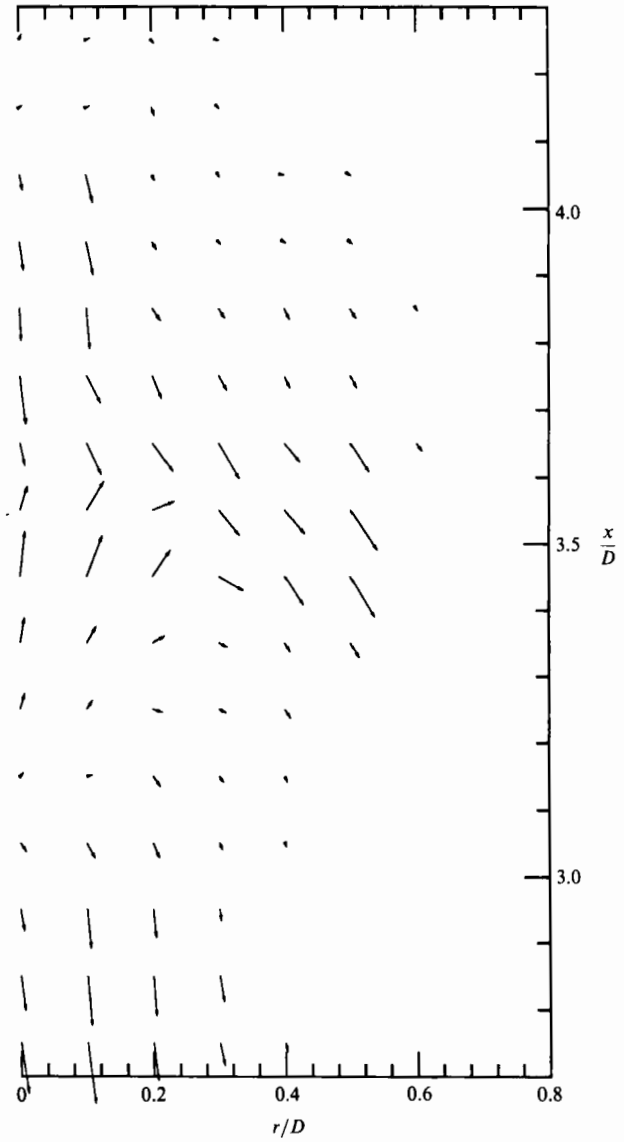

FIGURE 28. Phase-averaged particle number flux vectors, $\Phi = 0°$.

Frequency (Hz)	St_D	u'/U
218	0.30	0.11
364	0.51	0.11
510	0.71	0.020
648	0.90	0.020
794	1.10	0.008

TABLE 3. Forcing amplitudes for Jet 1, §4.2.4

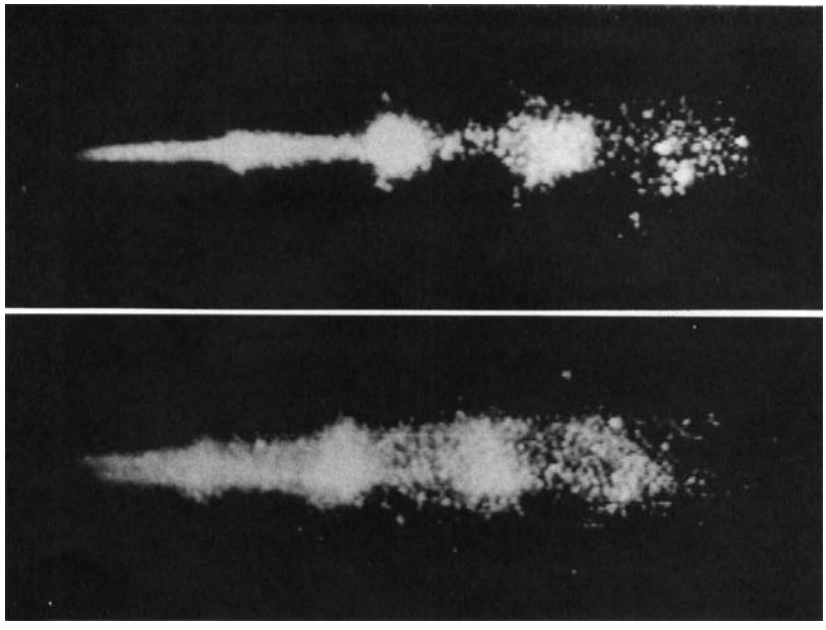

FIGURE 29. Variation of particle loading, $St_D = 0.3$, $M = 0.06$ (top), $M = 0.50$ (bottom).

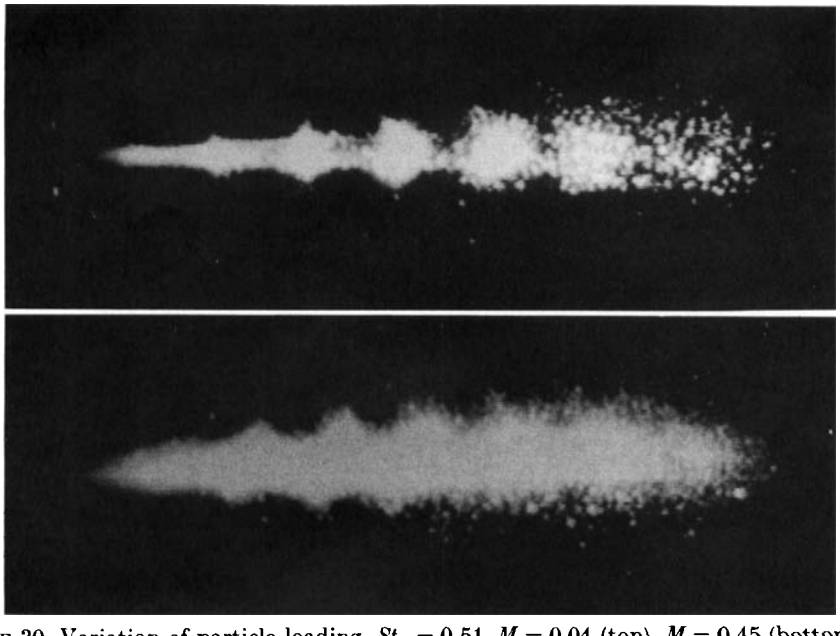

FIGURE 30. Variation of particle loading, $St_D = 0.51$, $M = 0.04$ (top), $M = 0.45$ (bottom).

4.2.4. *Variation of particle loading*

Experiments involving the variation of particle-to-air mass loading ratio were carried out using Jet 1 directed vertically downward. The jet Reynolds number was 19000, and the forcing frequencies and resulting velocity fluctuation amplitudes are listed in table 3. The mass loading ratio could be increased up to 1.0, but the jet flow became unsteady as a result of slugging in the fluidized bed feeder, and the flow

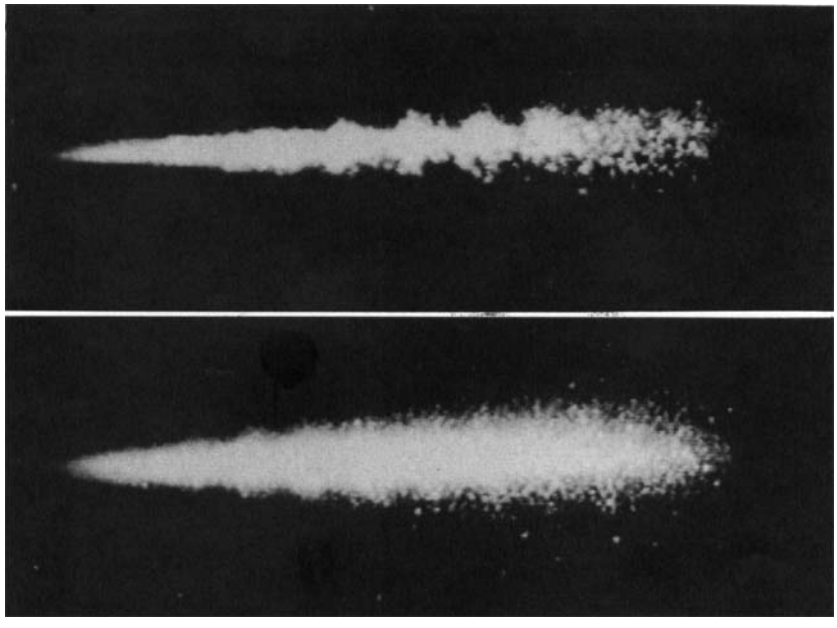

FIGURE 31. Variation of particle loading, $St_D = 0.71$, $M = 0.05$ (top), $M = 0.39$ (bottom).

conditions were difficult to reproduce. Therefore, no results above $M = 0.65$ are presented. Strobed visualization recorded on videotape was used to examine the flow structure. As the mass loading ratio was increased, the amount of light scattered also increased. To avoid saturating the videocamera at high M, a neutral density filter was attached to the camera lens, and the laser power and lens opening were decreased. Thus, absolute scattering intensities cannot be compared among different loading cases.

Results of the visualization studies are shown in figures 29–33. Each figure contains two photographs, one depicting a low M and one depicting a relatively high M (of the order of 0.5). For flow forced at $St_D = 0.30$, 0.51, 0.71 and 0.9, large-scale structures persist at the higher mass loadings. Particle clusters and 'structure' in the particle streams are clear. Also, the relative patterns of scattered light intensity are quite similar when the higher and lower M cases in each figure are compared. At the highest forcing frequency ($St_D = 1.1$), waviness in the particle distribution is present at low M, but hard to discern at higher M. In this high M photograph, periodic waviness is limited to one side of the particle stream near the nozzle exit. Thus, even at this higher frequency, it appears that flow structures persist up to moderate M.

It should be noted that Yang *et al.* (1990), who performed a stability analysis on a two-dimensional mixing layer seeded with a uniform distribution of particles, found that amplification rates of disturbances at all frequencies were smaller than those seen in a single-phase flow. This result suggests that in the round jet, initial vortex formation and later vortex pairing might be delayed by the presence of particles. (The present flow differs significantly from the modelled flow in that only one side of the mixing layer is seeded, the particles are not evenly distributed in the radial direction, and the particles and fluid are not in dynamic equilibrium near the nozzle exit.) Our experimental results show no evidence of any delay in particle cluster formation (hence vortex ring formation) for the forced cases described. Whether or not the structures are partially damped remains unknown since the flow

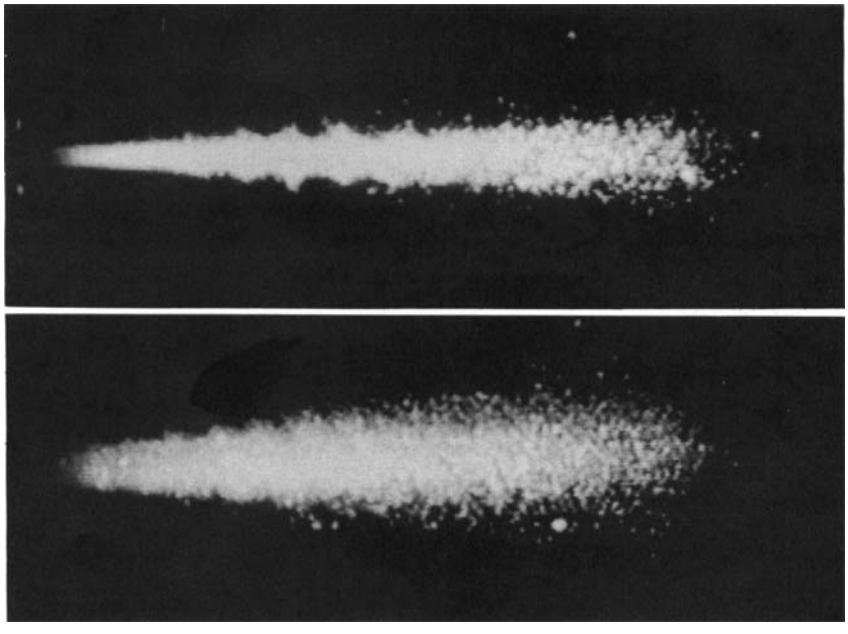

FIGURE 32. Variation of particle loading, $St_D = 0.90$, $M = 0.04$ (top), $M = 0.65$ (bottom).

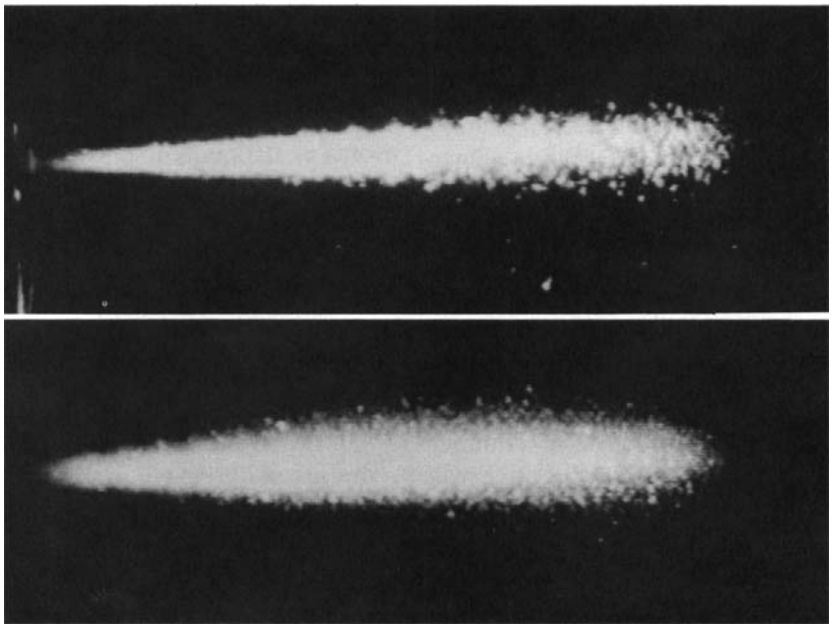

FIGURE 33. Variation of particle loading, $St_D = 1.1$, $M = 0.05$ (top), $M = 0.47$ (bottom).

visualization technique used was purely qualitative and insensitive to small changes in light scattering owing to small changes in jet structure. The lack of any merging of clusters over the axial range examined for either low or moderate particle loading is more likely to be due to strong fundamental forcing of the flow rather than to suppression of subharmonic instabilities by the presence of particles (refer to §4.2.1).

5. Discussion

To analyse the behaviour of the particle-laden jet in terms of the Stokes number, the appropriate scales for L_v and U_v must first be chosen. For the velocity scale, either a vortex propagation velocity or the tangential velocity at the outer edge of a vortex could be chosen. The vortex propagation velocity in the jet near field is assumed to be half the nozzle exit velocity. If a vortex ring is assumed to have a circular cross-section, and the tangential velocity around the cross-section is assumed to be constant, then the tangential velocity at the outer edge of the cross-section is also about half the nozzle exit velocity. Thus, it appears that $U_v = \frac{1}{2} U$ is a good choice for the fluid velocity scale.

The two most obvious choices for the eddy lengthscale are the diameter of the vortex core cross-section and the axial distance between adjacent vortex cores. The vortex core diameter is somewhat ill-defined and difficult to measure. Therefore, the spacing between the vortex cores is chosen as the appropriate fluid lengthscale. Based on the above scales, the values of γ calculated for the present study will correspond to approximately half of those reported by Chung & Troutt (1988).

In the near field of the unforced jet, a range of fluid timescales was present (refer to figures 4 and 5). In these two figures, U is 14.4 m/s so that U_v is 7.2 m/s. In the region up to $x/D = 3.8$, the vortex lengthscales L_v ranged from $0.26D$ to $1.2D$. Thus, the fluid timescale τ_f ranged from 0.72 ms to 3.3 ms. If τ_p is chosen as 21 ms ($d_p = 55\ \mu$m), the Stokes number varies between 29 and 7.2. Examining the distribution of particles in figure 5, we see that particles are drawn outward from the jet core region on the downstream side of the vortex centres at $x/D = 1.6$. At this position, the fluid timescale is 1.8 ms yielding a value of γ of about 12. The same behaviour occurs downstream of the larger vortices at later axial positions where γ is smaller. Thus, in this figure, $\gamma = 12$ constitutes the upper limit for which we see strong convection of particles by vortices. Note that although no particles are ejected from the jet by the smaller vortices upstream of $x/D = 1.6$, very few particles come near those vortices to begin with. If the particles were to encounter those vortices, the particle paths might be altered.

When the jet was forced at a single frequency, a range of vortex sizes and spacings could be generated by varying that forcing frequency. In §4.2.1, flow forced at Strouhal numbers from 0.26 to 0.93 was examined. The vortex velocity scale U_v was 8.5 m/s, and vortex lengthscales ranged from $0.67D$ to $2.6D$. Flow forced at $St_D = 0.43 + 0.21$, $\Theta = 0°$ yielded an even greater lengthscale of $3D$. The entire range of lengthscales produced Stokes numbers of 3.0–12. Over this range of γ, a range in particle distribution characteristics within the jet is observed. For low-frequency forcing (hence, large L_v and small γ), dense particle clusters form. The cross-sections of the clusters are shaped like arrowheads with the heads pointed in the downstream direction. Distinct tails are present on the upstream ends of the clusters where particles are thrown outward from the jet axis. Regions of relatively low particle number density are located between the clusters. This behaviour was observed from $3 < \gamma < 6.5$ (refer to figures 6, 7, and 14). This range of Stokes numbers corresponds most closely with the range seen in the mixing layer studies discussed in §1.

For $7 < \gamma < 11$ (see figure 8), clusters of particles are still present, but the clusters are much rounder in shape. Tails on the clusters owing to flinging of particles are not apparent. Also, the particle number density does not oscillate strongly as one moves downstream on the jet axis. For the range $11 < \gamma < 13$, the flow structures alter the particle paths, but distinct clusters do not form. (See figures 9 and 11.) In strobed

flow visualization studies where γ was greater than 13, no effects of flow structures on the particle distribution were observed.

The case of $Re_D = 19000$, $St_D = 0.51$ depicted in figure 10 and chosen for the velocity studies yields $\gamma = 6.5$ which is very close to Chung & Troutt's $\gamma_\tau = 10$ case (corresponds to about $\gamma = 5$ using our definition). It is interesting to compare results from the two studies. The phase-averaged LDA measurements in the present experiments yielded no evidence of particles moving toward the jet axis over the range $2.7 < x/D < 4.3$. Figures of particle distribution in the numerical study indicate that many particles which start at $r/D \approx 0.45$ eventually move closer to the jet axis. We suspect that our results do not show a similar effect because few particles in the experiment exit the jet nozzle at such a large radius. Indeed, very few particles starting at $r/D \approx 0.25$ in the simulation move inward. Also, it is possible in the experiment that particles have already moved inward before $x/D = 2.7$.

The numerical results of Chung & Troutt do not exhibit the strong axial variations in particle concentration seen in the experiments. Again, this is probably because of differences in initial conditions. In the present experiments, most particles exited the nozzle near the jet centreline. Therefore, a large percentage of particles was eventually directed toward particle 'stagnation' regions where dense clusters formed. Since the numerical study concentrated more on lateral dispersion, no results for particles initially located near the jet axis were presented.

The experimental jet with $\gamma = 6.5$ exhibited strong outward convection of particles from the regions immediately downstream of vortex rings. The simulation appears to show such dispersion beginning downstream of $x/D = 4$ for particles which started at large and medium radius. However, the simulation was stopped at this point, and the dispersion statistics were computed. It is highly possible that the particles in this case would eventually disperse further than the lighter particles depicted for $\gamma_\tau = 1$. The lighter particles appear to wrap around the vortex ring cores instead of being convected outward. Unfortunately, we do not have results comparable to the numerical simulation of the lighter particles. We would expect similar or enhanced clustering of these particles and similar outward ejection of particles to the limit where particles begin to wrap further around vortices.

Instantaneous variations in particle distribution owing to the presence of azimuthal flow structures were not examined in this set of experiments. Because the lengthscales involved in azimuthal variations are significantly smaller than the values of L_v, we expected that the effects of azimuthal or longitudinally-oriented structures on the given particles would be small. Separate experiments involving serrated nozzle attachments designed to deliberately perturb the jet's axisymmetry and generate longitudinal structures at fixed azimuthal locations (see Longmire *et al.* 1991; Longmire & Eaton 1990) showed some evidence of non-axisymmetric particle distributions. We expect that random azimuthal flow structures in a round jet containing particles of smaller time constant would have a significant effect on particle motion and distribution.

Analysis of the above results reveals two factors which are crucial to modelling particle flow in a gas continuum. The first factor is that the effects of large-scale structures and anisotropy in the continuous phase flow must be included. The studies on both unforced and forced jet flow showed that large-scale structures strongly affect particle distributions and velocities. Particles tend to become concentrated in areas of low vorticity and high strain. Also, particles move away from or never encounter areas of high vorticity such as vortex ring cores. In any particle-laden turbulence model where an instantaneous view of the flow is important (e.g. models

of combusting or reacting flow), then, large-scale anisotropic structures cannot be ignored.

The second factor which is important for any good model of a particle-laden flow is the set of initial conditions. In the present study, the initial distribution of particles in the round jet was highly non-uniform. Particles were heavily concentrated near the jet centreline owing to the effects of the contraction. The particle velocities exiting the contraction were also non-uniform as the particles away from the jet axis had negative radial velocities on average. Finally, the particle axial velocities lagged the fluid velocity significantly at the nozzle exit (also because of the contraction). These initial conditions must produce particle distributions in the flow which differ substantially from a flow with a uniform particle distribution and matching particle and fluid velocities at $x = 0$. In a flow with these idealized initial conditions, the effect of vortex ring structures on particle dispersion in the jet near field would probably be much stronger than that in the present experiments because more particles would encounter the rings sooner. However, in a realistic flow, the idealized initial conditions may not be achievable, and any model of the flow must accommodate this.

The results of the present experiments leave open the question of how to model the effects of particles on turbulence. We do know that moderate particle loadings do not eliminate large-scale vortical structures. We do not know the extent to which the particles may damp the structures (if at all). However, it is apparent that areas of high and low particle concentration are highly correlated with specific types of flow structures. Therefore, any model which attempts to include turbulence modulation effects should account for these correlations. For example, the effects of turbulence modulation are probably selective where certain turbulence lengthscales are enhanced or suppressed in the areas of high particle concentration.

6. Summary and conclusions

The flow structures in a lightly-loaded particle-laden jet are very similar to those in a single-phase jet. The near field of the particle-laden jet is dominated by axisymmetric vortex ring structures which roll up in the shear layer. The ring structures persist in jets with particle-to-air mass loading ratios of up to 0.65.

Results of flow visualization studies and quantitative number density measurements show that particle dispersion is dominated by convection by the coherent structures rather than by diffusion due to random three-dimensional turbulence. For appropriate fluid and particle timescales, the instantaneous concentration field of solid particles in the jet is strongly influenced by the vortex ring structures. Where large ring structures are present, the jet contains distinct regions of very high and very low particle concentration. Also, a larger percentage of particles are found in sparsely populated regions owing to particles being ejected away from the jet axis. Where smaller ring structures are present, dense clustering of particles does not occur, but the paths of some of the particles are affected by the structures. When two vortex rings pair, particle clusters associated with each ring also pair. This process yields regions of even higher particle concentration than those occurring downstream of individual large rings.

Phase-averaged velocity measurements provide insight into the mechanisms for the formation of the particle clusters and the dispersion of particles. Particles are dragged into the highly-strained regions from both upstream and downstream owing to local variations in the fluid velocity. Particles are then convected outward by the

outwardly moving fluid at these locations. Number flux measurements show that a very large percentage of particles are dispersed from the jet in these regions.

This work was funded by the Electric Power Research Institute under Contract RP 8005-2. E. K. L. was supported by fellowships from the Link Foundation and the American Association of University Women. The authors thank Dr G. S. Lewis and Professor Brian Cantwell for the use of their scanning hardware and software.

REFERENCES

BOUCHARD, E. E. & REYNOLDS, W. C. 1982 The structure and growth of the mixing layer region of a round jet. Rep. TF-17, Thermosciences Division, Dept. of Mech. Engng, Stanford University.

CHEIN, R. & CHUNG, J. N. 1987 Effects of vortex pairing on particle dispersion in turbulent shear flows. *Intl J. Multiphase Flow* **13**, 785–802.

CHUNG, J. N. & TROUTT, T. R. 1988 Simulation of particle dispersion in an axisymmetric jet. *J. Fluid Mech.* **186**, 199–222.

CROW, S. C. & CHAMPAGNE, F. H. 1971 Orderly structure in jet turbulence. *J. Fluid Mech.* **48**, 547–591.

CROWE, C. T., GORE, R. & TROUTT, T. R. 1985 Particle dispersion by coherent structures in free shear flows. *Particulate Sci. Tech.* **3**, 149–158.

DAHM, W. J. A. & DIMOTAKIS, P. E. 1987 Measurements of entrainment and mixing in turbulent jets. *A/AA J.* **25**, 1216–1223.

FLECKHAUS, D., HISHIDA, K. & MAEDA, M. 1987 Effect of laden solid particles on the turbulent flow structure of a round free jet. *Exps Fluids* **5**, 323–333.

HARDALUPAS, Y., TAYLOR, A. M. K. P. & WHITELAW, J. H. 1989 Velocity and particle flux characteristics of turbulent particle-laden jets. *Proc. R. Soc. Lond.* A**426**, 31–78.

KAMALU, N., WEN, F., TROUTT, T. R., CROWE, C. T. & CHUNG, J. N. 1988 Particle dispersion by ordered motion in turbulent mixing layers. *ASME Forum on Cavitation and Multiphase Flow*, pp. 150–154.

KOBAYASHI, H., MASUTANI, S. M., AZUHATA, S., ARASHI, N. & HISHINUMA, Y. 1987 Dispersed phase transport in a plane mixing layer. *2nd Intl Symp. on Transport Phenomena in Turbulent Flows, Tokyo*, pp. 693–706.

LAZARO, B. J. & LASHERAS, J. C. 1989 Particle dispersion in a turbulent plane shear layer. *Phys. Fluids* A **1**, 1035–1044.

LONGMIRE, E. K. & EATON, J. K. 1990 Structure and control of a particle-laden jet. Rep. MD-58, Thermosciences Division, Dept. of Mech. Engng, Stanford University.

LONGMIRE, E. K., EATON, J. K. & ELKINS, C. J. 1992 Control of jet structure by crown-shaped nozzles. *AIAA J.* **30** (to appear).

MAXEY, M. R. 1987 The gravitational settling of aerosol particles in homogeneous turbulence and random flow fields. *J. Fluid Mech.* **174**, 441–465.

MOSTAFA, A. A., MONGIA, H. C., MCDONELL, V. G. & SAMUELSEN, G. S. 1989 Evolution of particle-laden jet flows: a theoretical and experimental study. *AIAA J.* **27**, 167–183.

PETERSEN, R. A. & SAMET, M. M. 1988 On the preferred mode of jet instability. *J. Fluid Mech.* **194**, 153–173.

SQUIRES, K. D. & EATON, J. K. 1991 Measurements of particle dispersion obtained from direct numerical simulations of isotropic turbulence. *J. Fluid Mech.* **226**, 1–35.

YANG, Y., CHUNG, J. N., TROUTT, T. R. & CROWE, C. T. 1990 The influence of particles on the spatial stability of two-phase mixing layers. *Phys. Fluids* A **2**, 1839–1845.